Development of the Orion Crew Module Static Aerodynamic Database, Part II: Supersonic/Subsonic

Karen L. Bibb[*]
Eric L. Walker[†]
Gregory J. Brauckmann[‡]
NASA Langley Research Center, Hampton, VA 23681

Philip E. Robinson[§]
Johnson Space Center, Houston, TX

This work describes the process of developing the nominal static aerodynamic coefficients and associated uncertainties for the Orion Crew Module for Mach 8 and below. The database was developed from wind tunnel test data and computational simulations of the smooth Crew Module geometry, with no asymmetries or protuberances. The database covers the full range of Reynolds numbers seen in both entry and ascent abort scenarios. The basic uncertainties were developed as functions of Mach number and total angle of attack from variations in the primary data as well as computations at lower Reynolds numbers, on the baseline geometry, and using different flow solvers. The resulting aerodynamic database represents the Crew Exploration Vehicle Aerosciences Project's best estimate of the nominal aerodynamics for the current Crew Module vehicle.

Nomenclature

C_x	A force or moment coefficient
C_A	Axial force coefficient
C_D	Drag force coefficient
C_L	Lift force coefficient
C_m	Pitching moment coefficient
$C_{m_{apex}}$	C_m, resolved at vehicle theoretical apex
$C_{m_{cg}}$	C_m, resolved at cg location
$C_{m_{cgx}}$	C_m, resolved at mrc along centerline
C_N	Normal force coefficient
C_n	Yawing moment coefficient
cg	Center of gravity
d_2	Bias correction factor for range-based standard deviation
FMV	Blended velocity function
k	Coverage factor, $\sqrt{3}$
$kfps$	Thousand feet per second
L/D	Lift-to-Drag ratio
M	Database cardinal Mach number
MI	Margin Index
M_∞	Freestream Mach number
mrc	Moment reference center
Re_D	Reynolds Number based on vehicle diameter
$\overline{R_i}$	Range of data for condition i
sf	Smoothing factor
uC_x	Uncertainty in a force or moment coefficient
UF_{C_x}	Database uncertainty factor for a force or moment coefficient
U_∞	Freestream velocity
α	Angle of attack, deg.
α_T	Total Angle of attack, deg.
β	Sideslip Angle, deg.
ϕ	Roll Angle, deg.
δ	Increment or range to cover
σ	Standard deviation

Subscripts

$5sp$	Five species air
alt	Altitude

---

[*] Research Engineer, Aerothermodynamics Branch, Senior Member AIAA
[†] Research Engineer, Configuration Aerodynamics Branch, Senior Member AIAA
[‡] Research Engineer, Aerothermodynamics Branch, Associate Fellow AIAA
[§] Aerospace Engineer, EG311 Division

bal	Balance accuracy
c2c	OVERFLOW to USM3D comparisons
cfd	CFD variations
chem	Chemistry model differences
flt	Flight Reynolds number
hs	Heatshield asymmetry
idat	IDAT backshell angle change
interp	Interpolation
lam	Laminar
ltp	Laminar-turbulent variations
ovf	OVERFLOW
pg	Perfect gas air
Re	Reynolds number variation
RR	Repeatability
turb	Turbulent
wt	Wind tunnel data variations
wt2cfd	Wind tunnel to CFD variations
wtRe	WT Reynolds number

I. Introduction

The Apollo-derived Orion Crew Exploration Vehicle (CEV) was designed by NASA and its industry partners within the now-cancelled Constellation Program as part of the Agency's Exploration Mission, and was intended to be the foundation for manned exploration of the Moon, Mars, and beyond.[1,2] The Orion CEV design is now the reference vehicle for the development of the Multi-Purpose Crew Vehicle (MPCV), the exploration vehicle that will carry crew to space, provide emergency launch abort capability, sustain the crew during the space travel, and provide safe re-entry from deep space return velocities.[3,4] The CEV (and now the MPCV) consists of the Crew Module (CM), Service Module, Spacecraft Adapter, and Launch Abort Tower, as shown in Figure 1. The Orion CM is similar in shape to, but larger than the Apollo capsule. A test flight planned for late 2013, designated Orion Flight Test 1 (OFT-1), will focus on the entry phase of flight for the CM.

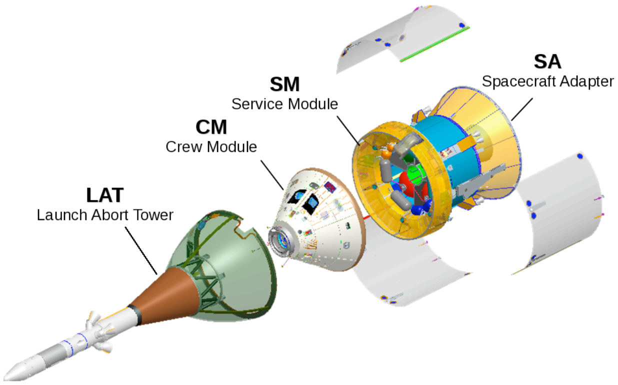

Figure 1: Orion Crew Exploration Vehicle components.

The Orion aerodynamic database[5,6] has been developed by the CEV Aerosciences Project (CAP), and is regularly updated with improvements to the aerodynamic modeling of various systems. The primary function of the database is to provide aerodynamic data to the trajectory simulations that are used to develop the guidance, navigation, and control systems for the vehicle and provide targeting and landing ellipse prediction during flight operations. The aerodynamic database development process is shown notionally in Figure 2. Note that this paper will use the term aerodatabase throughout to refer to the Orion aerodynamic database. The CAP team provides this data through an API (Application Programming Interface) that is integrated into the trajectory simulation tools. The API uses tabulated nominal and uncertainty aerodynamic data to compute and return the aerodynamic forces and moments acting on the vehicle at the desired vehicle state. The tabular data is developed from various computational and experimental sources. Uncertainties due to turbulence modeling, grid resolution, wind tunnel repeatability, and other physical modeling are combined to provide tabulated database uncertainties. The CAP database covers the aerodynamics for all phases of the vehicle flight beginning with the separation from the launch system (including nominal and abort situations) until the CM re-enters the atmosphere and lands.

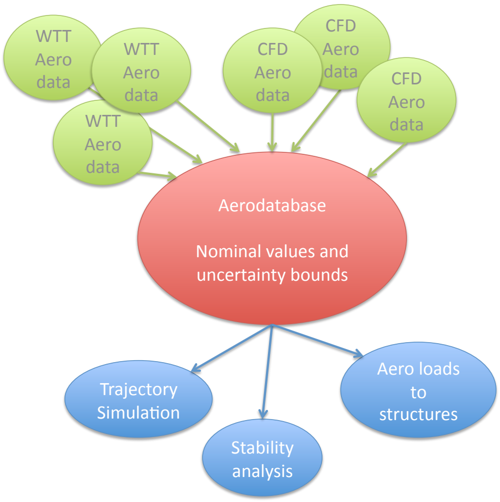

Figure 2: CAP aerodatabase development process.

This paper describes the general process of developing the nominal static aerodynamic coefficients and uncertainties for the subsonic through low hypersonic flight regimes for the Orion Crew Module ($M_\infty \leq 8$), The process described reflects the current best estimate of the database, and discusses areas where further work is planned to support the first entry test flight of the Orion vehicle. This paper covers the full angle-of-attack range for the vehicle, $0^\circ \leq \alpha \leq 180^\circ$, for $M_\infty \leq 8$. A companion paper[7] covers the database development for $M_\infty > 8$.

The available data, both experimental (WT) and computational (CFD), are discussed, with particular attention paid to comparisons between the various data sets. The basic process for combining the available data into a single data set varying in Mach and angle of attack is outlined, and some examples of the blending will be shown. The formulation of the uncertainties and development of each term is discussed, with particular attention paid to the Reynolds number variations and CFD to WT comparisons. The final database nominal coefficients with uncertainties are compared to the available data and vehicle trim characteristics are presented.

II. Database Inputs

II.A. Orion Crew Module Geometry

The nominal analytical Orion CM geometry is based on the Apollo configuration, and is shown in Figure 3. The spherical heatshield and conical backshell have been scaled to a maximum diameter of $198\,in$ compared to Apollo's $154\,in$. The CEV apex is truncated to accommodate docking hardware.

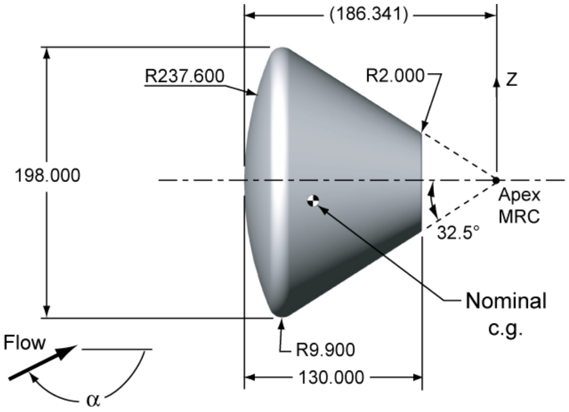

Figure 3: Dimensions of the smooth, axi-symmetric baseline Orion Crew Module, in inches.

The flight geometry is still being developed, and departs from the nominal, axisymmetric geometry in several key areas. The aerodatabase addresses these geometry differences by incorporating additional analysis to adjust the nominal coefficients and using uncertainties to cover expected variations. The geometry variations fit into three main categories.

First, the nominal 32.5° backshell angle was widened by 2.5° (to 30°), moving the theoretical apex further from the vehicle base, as shown in Figure 4. This modification provides more packaging volume for the parachute system and is referred to as the IDAT geometry[a]. Initial experimental and computational data were generated on the axisymmetric nominal geometry. Subsequent computational studies on the IDAT geometry have been performed, and the effect of incorporating the backshell angle change into the database is covered below.

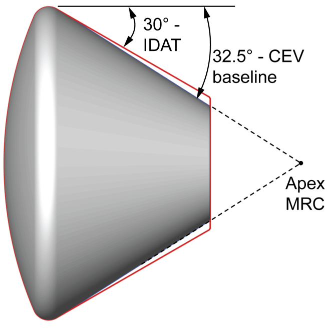

Figure 4: Dimensions of the axi-symmetric baseline Orion Crew Module.

The second major departure from the nominal geometry was reshaping the heatshield to minimize the thickness of the thermal protection system (TPS), resulting in an asymmetric heatshield shape. Conceptually, the shape is designed to be thicker in the higher heating regions such that the expected ablation drives the shape closer to the nominal spherical shape, and implies that the effect of the asymmetry will be greatest at the highest entry speeds. While this shape is still evolving, there have been some studies to address the aerodynamic effect. The studies have been primarily at hypersonic conditions, and are briefly discussed below in the uncertainty section.

The last group of geometry variations include features such as footwells, windows, steps in backshell tile thicknesses, and other protuberances. The aerodynamic effects of these relatively small features have not been quantified, and are assumed to be accounted for within the uncertainty model, as discussed further in the uncertainty section.

---

[a] The effort to redesign the packaging and deployment schedule for the parachute system was called the Integrated Design Assessment Team, and the resulting changes to the CM vehicle are generically called the IDAT geometry.

II.B. Crew Module Coordinate System Conventions

The CM coordinate system, angle of attack, and aerodynamic coefficient orientation conventions are shown in Figure 5, taken from the CEV Aerodynamic Databook.[5] Note in particular that a heatshield-forward attitude has an angle of attack of 180°.

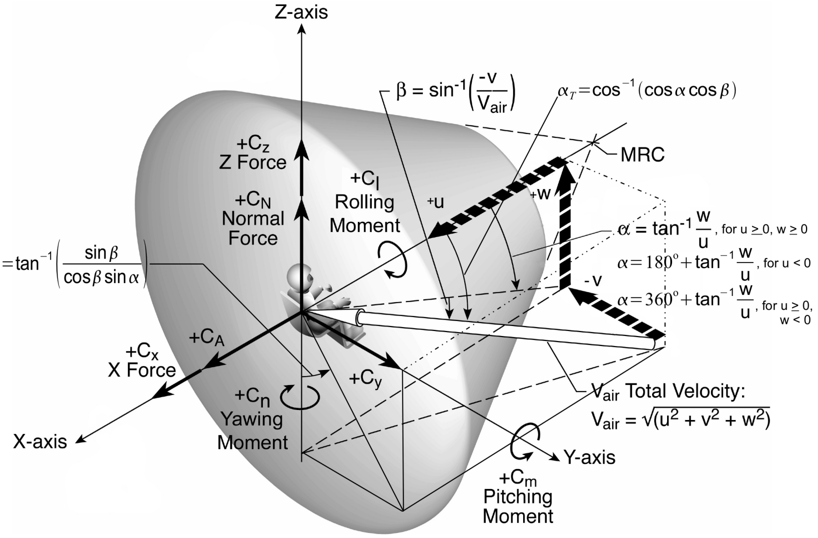

Figure 5: Axis, Force, and Moment Definitions for Crew Module.[5] Astronaut, shown for orientation purposes, is not to scale.

The aerodynamic moments are typically resolved about a nominal *cg* location defined by the Orion Project. Through the course of the CM development, the nominal *cg* location has shifted, primarily providing progressively smaller offsets of the *cg* location in the *z-axis* direction. The CAP team typically considers moments resolved about three different *mrc* locations: apex, *cg*, and symmetric *cg*. The database is provided with the moment about the theoretical apex for the nominal, 32.5° backshell, geometry (labeled MRC in Figure 5). The flight *cg* location is used to determine flight characteristics such as trim angle of attack, and is provided as an output of the API. The symmetric *cg* (a location along the *x-axis* corresponding to the *cg* with no *y-* or *z-axis* offsets) is used to develop the nominal pithching-moment coefficient so that symmetry conditions can be enforced. Moment uncertainties are developed for either the *cg* or symmetric *cg* location.

II.C. CM Database Formulation

The CM portion of the database provides the aerodynamic forces and moments as a function of a velocity parameter, *FMV*, and the orientation of the vehicle with respect to the flow. The database formulation takes advantage of the fact that the vehicle is primarily axisymmetric and treats the nominal coefficients as functions of FMV and α_T only. Tables are provided for C_A, C_N, and C_m, and transformations made to compute the full set of coefficients. The velocity parameter, FMV, is defined in Equation 1 as

$$FMV = \begin{cases} M_\infty & \text{if } U_\infty \leq 8.8\,kfps \\ M_\infty(9.8 - U_\infty) + U_\infty(U_\infty - 8.8) & \text{if } 8.8\,kfps < U_\infty < 9.8\,kfps \\ U_\infty & \text{if } U_\infty \geq 9.8\,kfps, \end{cases} \tag{1}$$

where U_∞ is given in units of *kfps*. The FMV function provides a single velocity parameter for the entire database by taking advantage of the near numerical equivalency of Mach number and velocity (in *kfps*) around Mach 10[b]. The blended parameter provides a smooth transition between Mach number for subsonic and supersonic speeds and velocity for hypersonic speeds. For the development of the database for $FMV \leq 8$, Mach number and *FMV* are used interchangeably.

---

[b] Note that the formulation of *FMV* complicates the direct application of the Orion aerodatabase to entry simulations in other atmospheres, such as at Mars.

Because the vehicle is predominately axi-symmetric, the database formulation treats the nominal coefficients as functions of FMV and α_T only. Tables are provided for C_A, C_N, and C_m, and transformations made to compute the full set of nominal coefficients.

The database API computes dispersed aerodynamic coefficients based on the data in the uncertainty tables. In order to facilitate development of dispersed trajectory simulations (typically Monte Carlo based), the user provides an uncertainty factor for each uncertainty coefficient, and the nominal and uncertainty values are combined to form the dispersed coefficient. For a particular simulation within a dispersed trajectory simulation, the user provides an uncertainty factor, typically in the range $-1.0 \leq UF_{C_x} \leq 1.0$, which will be applied to the aerodynamics for that simulation. An uncertainty factor of zero will return the nominal coefficient for C_x, and $UF_{C_x} = 1.0$ will return the nominal plus the total uncertainty for C_x. For the Orion database, all uncertainties are specified as uniform uncertainties except for the rolling moment uncertainty which is treated as a normal distribution. This means that the uncertainty factors chosen for the dispersed trajectory set will be chosen based on a uniform distribution from -1.0 to $+1.0$.

Table 1 specifies the database tables required for the CM static aerodynamics, and lists the independent parameters for each table. Details of how the data from the tables are built into the final aerodynamic coefficients can be found in the companion paper,[7] and more fully in the Orion Formulation Document[6]

Table 1: Database tables and arguments for the CM static aerodynamics.[6]

Nominal Tables			Uncertainty Tables		
Coefficient	Table Name	Table Arguments	Coefficient	Table Name	Table Arguments
C_A	`CACM`	FMV α_T	uC_D	`UCDCM`	FMV α_T
C_N	`CNCM`	FMV α_T	uC_L	`UCLCM`	FMV α_T
			$u(L/D)$	`ULODCM`	FMV α_T
$C_{m_{apex}}$	`CMCM`	FMV α_T	$uC_{m_{cg}}$	`UCMCGCM`	FMV α β
			$uC_{n_{cg}}$	`UCLNCGCM`	FMV α β
			$uC_{l_{cgx}}$	`UCLLCM`	FMV

II.D. Available Experimental Data

The primary experimental data available for $M_\infty \leq 8$ come from three tests conducted early in the project: 05-CA[8] in the Ames Unitary Plan Wind Tunnel (AUPWT), 03-CA[9] in the Langley Unitary Plan Wind Tunnel (LaUPWT), and 09-CA[8] in the Langley Aerothermal Laboratory's Mach 6 facility. There have been several additional tests, for the LAV configuration and dynamic CM testing, that have generated static aerodynamic data on the CM, and have been used in developing uncertainties. A summary of the available test data on the CM is given in Table 2.

The 05-CA test used both a small (3.0%-scale) and large (7.7%-scale) model tested in both the the 11ft and 9x7 legs of the AUPWT. The test covered an angle of attack range from 142° to 172°, for $0.3 \leq M_\infty \leq 2.5$ and $1.0\text{x}10^6 \leq Re_D \leq 5.3\text{x}10^6$. Additional data was obtained for $M_\infty = 0.5$ at $Re_D = 7.0\text{x}10^6, 7.6\text{x}10^6$ and for $M_\infty = 1.6, 2.5$ at $Re_D = 0.5\text{x}10^6$. The data from 05-CA with the large model at the highest available Reynolds number were used in the database development. The 03-CA test utilized the 3.0%-scale model tested in the LaUPWT over an angle-of-attack range of 140° to 170° for Mach numbers 1.6, 1.8, 2.0, 2.5, 3.0, and 4.5, and Reynolds numbers of $0.5\text{x}10^6$, $1.0\text{x}10^6$, and $1.5\text{x}10^6$ based on body diameter. The data for $M_\infty \geq 2.5$ and $Re_D = 1.5\text{x}10^6$ from 03-CA are utilized in the database. The only hypersonic aerodynamic test, 09-CA, was run in Langley's 20-Inch Mach 6 Air facility, and covered the full range of angle-of-attack, -5° to 185°, and $Re_D = 1.0\text{x}10^6$. This test was run with an apex cover on to provide a geometry similar to Apollo, and without the apex cover for the CEV configuration. Murphy *et al.*[10] cover the details of these tests and provides discussion of the data including Mach and Reynolds number effects that guide how the data is used in the database.

Table 2: Available experimental data for CEV CM, $M_\infty \leq 8.0$.

Test	Ref	Facility	Mach	α range	$Re_D, 10^{-6}$	notes
03-CA *	**9, 10**	**LaRC UPWT**	**1.6 - 4.0**	**140°-170°**	**1.0 - 3.0**	**3.0% scale**
05-CA *	**8, 10**	**Ames 11 ft**	**0.2 - 1.4**	**142°-172°**	**max 5.3**	**7.7% scale**, 3% scale
		Ames 11 ft	**0.5**	**142°-172°**	**max 7-7.5**	**7.7% scale**, 3% scale
		Ames 9x7	**1.6 - 2.5**	**142°-172°**	**max 5.3**	**7.7% scale**, 3% scale
09-CA *	**10, 11**	**LaRC 20-Inch Mach 6**	**6.0**	**-5°-185°**	**1.0**	**2.02% scale, apex cover off** / on
24-AA	12	AEDC 16T	0.3 - 1.2	142°-172°	1.0	Re_D too low, asymmetric CM geometry
25-AA	12	Ames	1.6 - 2.5	142°-172°	0.75	Re_D too low, asymmetric CM geometry
27-AD	13, 14	LaRC TDT	0.2 - 1.1	142°-172°	1.0-5.0	Dynamics test, sting interference issues
61-AA	15	LaRC 14x22	0.13	142°-172°	1.0	Re_D too low, asymmetric CM geometry

---

* Data used for CM static aerodynamic database development.

II.E. Available Computational Data

The available computational data for the CM comes from several CFD solvers and covers both the baseline geometry with the 32.5° backshell angle and the IDAT geometry with the 30° backshell angle. The data sets with their respective Mach number and angle-of-attack ranges are summarized in Table 3.

Table 3: Available computational data for CEV CM, $M_\infty \leq 8.0$

CFD Solver	Backshell Angle	Mach number range	α range
Overflow	32.5°	0.2, 0.3, 0.5, 0.7, 0.9, 1.1	0°– 180°
Overflow	30° (IDAT)	0.3 – 8.0	0°– 180°
Usm3d	30° (IDAT)	0.5, 0.7, 0.9, 1.2, 2.5, 8.0	0°– 180°
Laura, Dplr	32.5°, 30°	2.0 – 8.0	150°– 172°

There are 2 primary sets of CFD data for the CM, both generated with the Overflow[16–19] solver using the SST turbulence model. Both primary data sets cover the full angle of attack range, $0° \leq \alpha \leq 180°$, with the point distribution highest in the trim region. The first set is for the nominal axisymmetric geometry, and are available for $M_\infty = 0.2, 0.3, 0.5, 0.7, 0.9,$ and 1.1. There is a corresponding set of computations on the IDAT geometry with the wider backshell angle. These computations cover the full Mach range to $M_\infty = 8.0$. The IDAT geometry cases were used for the nominal coefficient development.

The nominal backshell angle data set includes computations at both wind tunnel and flight Reynolds numbers, as well as some with a sting configuration matching the 27-AD test. There was considerable duplication in this set, with cases run on similar grids with the same solver options by multiple researchers. These duplicate cases were treated as repeat solutions to aid in the development of uncertainty. The cases with multiple Reynolds numbers were also used in the uncertainty development to cover the range of Reynolds numbers seen in flight, particularly subsonically.

An additional set of computations at selected Mach numbers and angle-of-attack ranges for the IDAT geometry were made using the unstructured package TetrUSS,[20–22] which is comprised of the Vgrid meshing package and Usm3d flow solver. The flow conditions overlap with the Overflow IDAT set and the computations have been utilized in the uncertainty development.

As Mach number increases into the hypersonic regime, real gas effects become a significant factor in the aerodynamics; these are not modeled either in the wind tunnel or with the primary Overflow data sets. For the higher Mach numbers ($M_\infty > 2$), a limited set of computations from the Laura[23,24] and Dplr[25–27] solvers has been used for nominal coefficient development in the trim region where appropriate, and for uncertainty quantification for real gas, altitude, and laminar-turbulent variations for $2 \le M_\infty \le 8$. This data set was developed by the CAP Aerothermal team as part of their efforts to characterize heating on the CEV, and is referred to in this paper as the aerothermal data set. These computations cover velocities above Mach 2, angles of attack between $150° < \alpha < 172°$, and a range of altitude conditions. For $M_\infty > 8$, the aerothermal data is the primary data source, and so including this data at the higher Mach numbers facilitates blending between the two regions of the aerodatabase. Note that the data used for nominal and uncertainty development is the average of a laminar and a turbulent solution at the same conditions, and is referred to in this paper as a *ltp* data point. More details on the full aerothermal data set can be found in the companion paper[7] which covers the hypersonic aerodynamic database development.

II.F. Data Coverage, Angle of Attack

The aerodatabase by design covers the entire range of orientation for the CM, such that α varies from 0° to 360°, and β from -90° to 90°. When the coefficients are axisymmetric, α_T varies between 0° and 180°.

Figure 6(a) shows the various available data sets, computational and experimental, for the full range of Mach number and angle-of-attack. The trim region for $M_\infty < 1.6$ is shown in Figure 6(b). The gray symbols and lines show the points in the database tables for the portion of the CM database covered in this paper. The wind tunnel data are shown in thick lines in shades of blue. The Mach 6 data from the 09-CA test can be seen to extend over the full angle-of-attack range, while the 05-CA and 03-CA data are only in the trim region, for $M_\infty \le 4$. The CFD for the baseline geometry, shown by the blue squares, are duplicated in most, but not all, cases by the IDAT CFD data. The orange diamonds are the primary Overflow IDAT CFD data used for the nominal development. The purple triangles are the duplicate points computed with Usm3d, and are only available for selected Mach numbers and limited angles of attack.

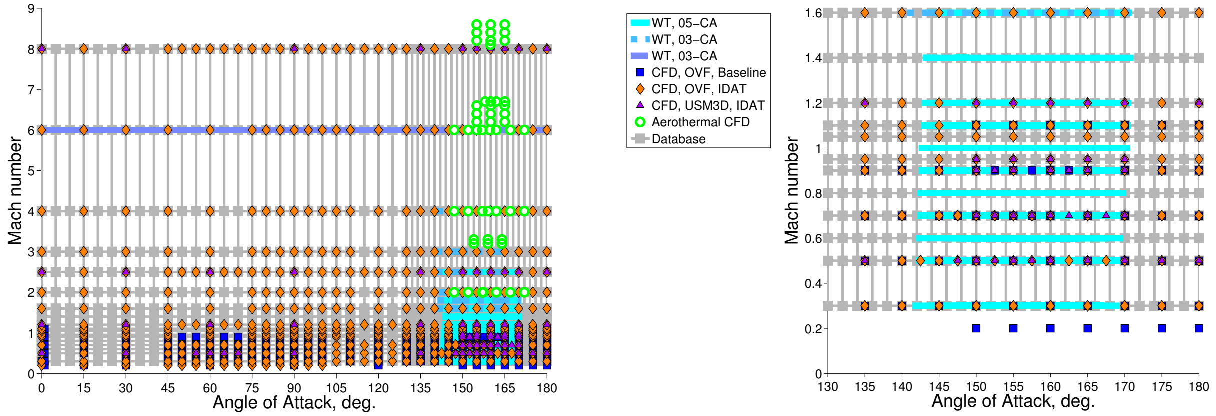

(a) $M_\infty \le 9,\ 0° \le \alpha \le 180°$

(b) $M_\infty \le 1.6,\ 130° \le \alpha \le 180°$

Figure 6: Mach number and angle-of-attack range coverage for all available data.

Typical nominal entry and abort trajectories fly in a tight angle-of-attack range, trimming in a 10° range subsonically and a 7° range hypersonically with full uncertainties applied. This range is located somewhere between 145° and 175° depending on the nominal *cg* location, with the nominal trim angle of attack closer to 180° as the *z-cg* location is closer to the vehicle centerline. The clustering of CFD points and concentration of the experimental data reflect the need for the best definition of the aerodynamics for this angle-of-attack range. At the lower subsonic speeds, the dynamics become very important, with the vehicle experiencing large oscillations about the trim point. The total angle of attack, α_T, can be as low as 120° below Mach 0.5. This implies that there is a broad range of angles-of-attack and sideslip angles that must be well-covered in the lower speed ranges, and therefore a denser CFD angle-of-attack distribution for subsonic Mach numbers. Below $\alpha = 45°$ there is a very sparse distribution in CFD data. For normal operations, the vehicle should not fly in this region.

II.G. Reynolds Number Coverage, Trajectory Envelope

The available data is limited in the variation in Reynolds number, particularly for the experimental data. Historical Apollo data[28–36] and the current CFD computations suggest that variation in the aerodynamics (particularly drag) continues as Reynolds number increases beyond the $Re_D = 5.3\,\mathrm{x}\,10^6$ available with the CEV WT data for subsonic Mach numbers. Figure 7 shows the drag coefficient for the current data set at $M_\infty = 0.7$ compared to relevant Apollo WT and flight data, for $\alpha > 140°$. The primary 05-CA data, at the highest WT Reynolds number, are shown as the cyan circles, and lie in the middle of the available data. The lower Reynolds number data from 05-CA, yellow circles, has a higher drag. The Apollo WT data (+ symbols), collected from various tests, is consistent with the current CEV data, with the higher Reynolds number data showing lower drag. Note that the $Re_D = 13\,\mathrm{x}\,10^6$ data is mingled with the lower $Re_D = 8\,\mathrm{x}\,10^6$ data, and that there is a large scatter in both sets. The Apollo flight data, from 3 of the early test flights, shows higher drag than most of the data. This pattern is consistent with other Mach numbers. The CFD data has generally lower drag than the experiment, and the low Reynolds number CFD shows higher drag than the high Reynolds number CFD. This pattern shown here for $M_\infty = 0.7$ is consistent with other subsonic Mach numbers, and begins to show the difficulties in modeling the aerodynamics in the angle-of-attack range in which the vehicle trims. Differences between the current WT data and the CFD are discussed in the next section.

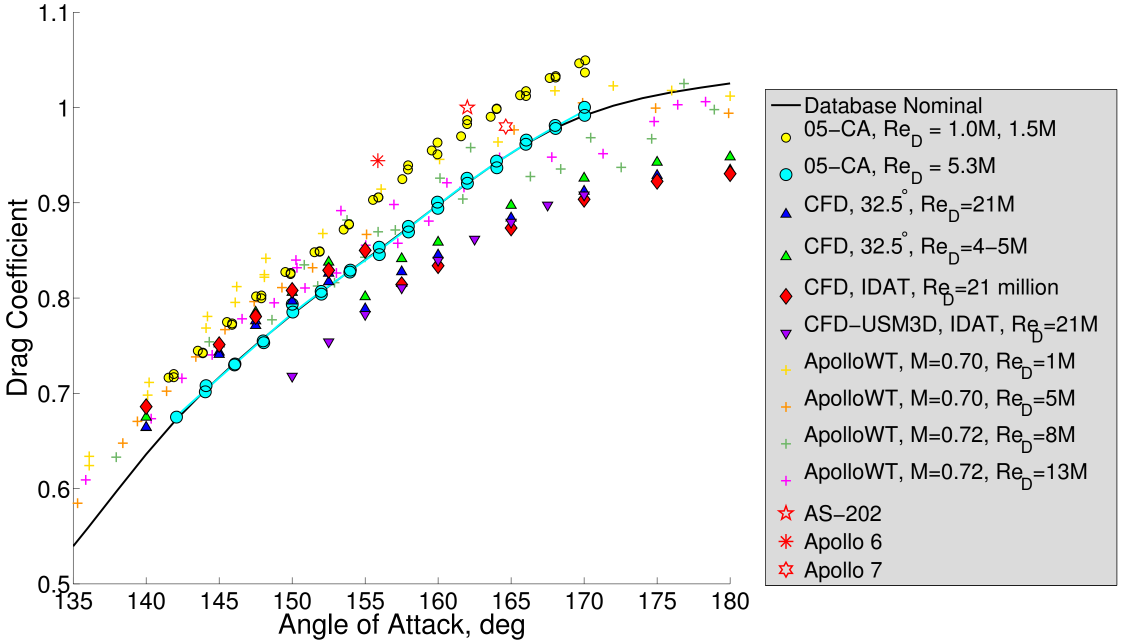

Figure 7: Available experimental and computational data for $M_\infty = 0.7$, compared to historical Apollo WT and flight data.

The Reynolds number range for the available computational and experimental data are shown in Figure 8, with representative entry and abort trajectory data[c] shown by the dark and light gray lines, respectively. Because the vehicle must be capable of performing an abort at any point along the ascent trajectory, the range of altitude conditions that the CM might experience is large. This is shown in Figure 8 by the large spread in Reynolds number at any given Mach number. The nominal entry trajectories have a much smaller spread in Reynolds number. Note that trajectories shown here are intended to show general trends, and are not necessarily equivalent to the final flight profiles.

---

[c] Monte Carlo sets of trajectories provided by the Orion Ascent Abort and Entry Mode Teams.

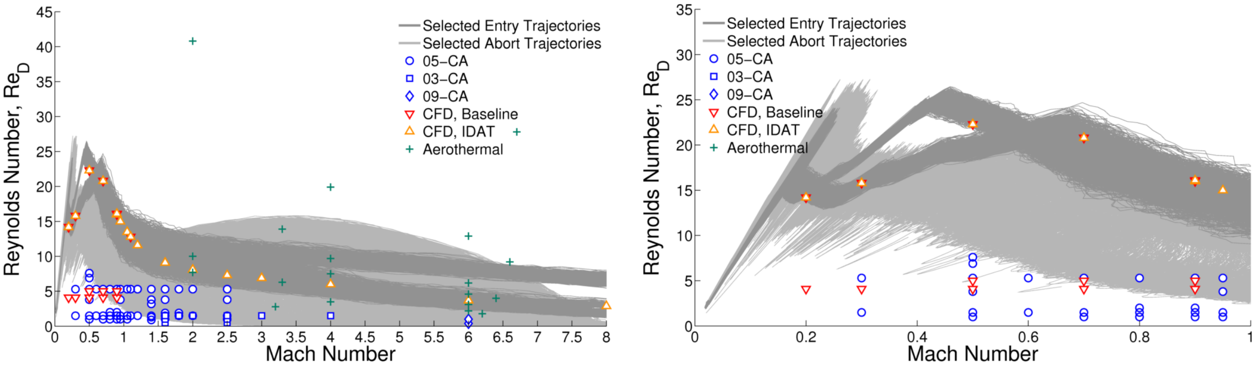

(a) Full Mach Range, $M_\infty < 8$

(b) Subsonic Mach Range

Figure 8: Reynolds Number (Re_D) vs. Mach number for selected entry and abort trajectory sets.

The available WT data, with a maximum $Re_D = 5.3 \,\mathrm{x}\, 10^6$ (except at $M_\infty = 0.5$), is below the nominal entry trajectory Reynolds number for all Mach numbers, and on the bottom edge of the abort trajectories subsonically. This lack of coverage of the trajectory space in Reynolds number is particularly problematic for the subsonic Mach numbers, were the CFD data predicts significant differences between the WT and flight Reynolds number computations. This suggests that the WT data at the highest Reynolds numbers have not reached Reynolds number independence. The problem is compounded because the CFD does a poor job of matching the WT data for the WT conditions. The approach for the database development has been to use the highest Reynolds number WT data as if it were equivalent to the flight Reynolds number, and account for a level of Reynolds number variation within the uncertainities.

The lack of coverage in the WT data for flight Reynolds number is less of a problem above Mach 1. The WT data show less variation with Reynolds number, and much of the lower range of the trajectory space is covered by the data. Above Mach 1, the primary CFD is available only for the flight Reynolds number.

Above Mach 3, the aerothermal data set covers the Reynolds number range fairly well, due to the range of altitude conditions considered by the aerothermal team. As will be shown later in the paper, the magnitude of the variation in aerodynamic quantities due to altitude variation is small, but measurable, and is accounted for in the uncertainty model.

II.H. Subsonic WT and CFD Data Comparisons

For the CM, the subsonic trim region has been the most difficult aerodynamic environment to develop. As discussed in the preceding sections, the wind tunnel conditions cover a much lower Reynolds number range than is seen in flight, and this prompts concerns over how well the data extends to actual flight. The CFD data show large discontinuities in drag at particular M_∞-α combinations that are not seen in the wind tunnel data, and this lowers confidence in how well the CFD is modeling the large, unsteady, separated base flow region which is dominated by difficult to model turbulence effects.

Figure 9 shows the available drag coefficient data for several Mach numbers. For $M_\infty = 0.3$, the CFD at WT Reynolds number (left triangle) compares well with the experimental data, and is higher than the CFD at flight Reynolds number. There is significant variation between the repeated CFD cases (on the baseline geometry) as well as for the IDAT geometry. For $M_\infty = 0.5$, the CFD results are even more varied, and the OVERFLOW IDAT computations show a jump in drag around $\alpha = 155°$. The differences between the computations at WT and flight Reynolds number again show a significant difference, although the flight Reynolds number data line up with the WT data for this Mach number. At $M_\infty = 0.9$, the Reynolds number differences are small, but the jump in drag is seen in all of the computations except those with USM3D. The discontinuity in drag goes away above Mach 1. At $M_\infty = 1.2$, the computational data is smooth again, but the drag is higher than the WT. As Mach number increases further, the agreement between WT and CFD data are improved, and the CFD data does not exhibit the instabilities seen at lower Mach numbers.

The details of the computational solutions and the ongoing efforts to improve the agreement of the solutions with the WT data are explored in both Stremel *et al.*[37] and McMillin *et al.*,[38] for the OVERFLOW and USM3D computations, respectively. Murphy *et al.*[10] provides more detail on the subsonic Reynolds number variations in the experimental data. At this time, a wind tunnel test in NASA Langley's National

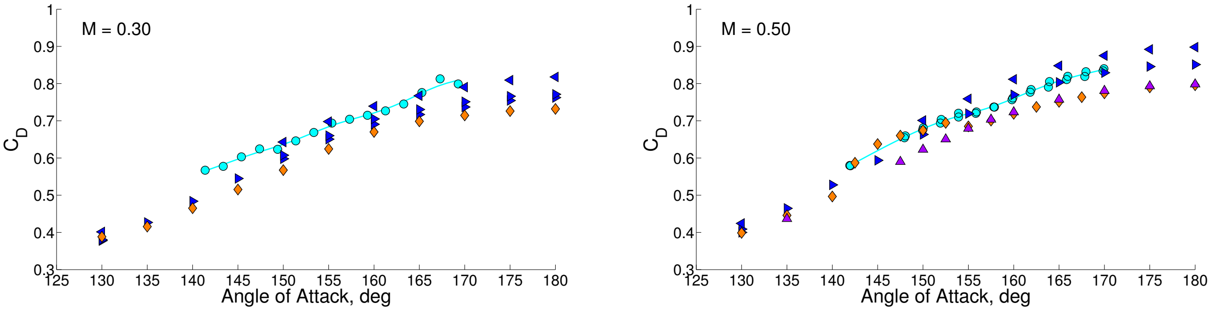

(a) $M_\infty = 0.3$ (b) $M_\infty = 0.5$

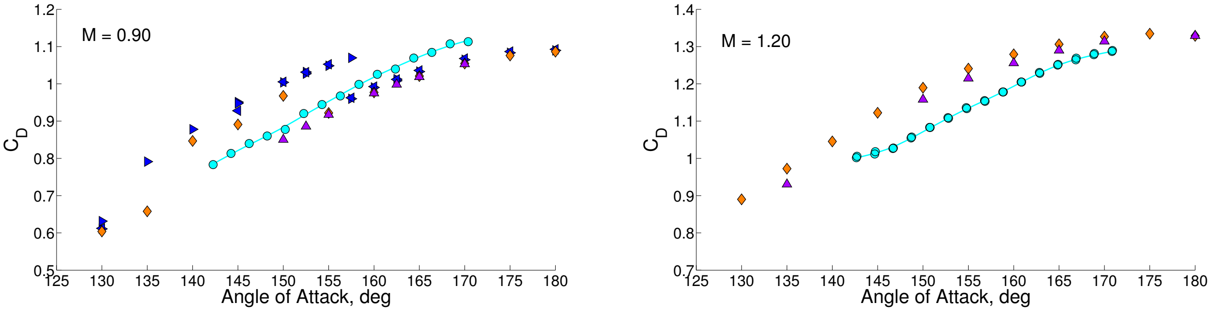

(c) $M_\infty = 0.9$ (d) $M_\infty = 1.2$

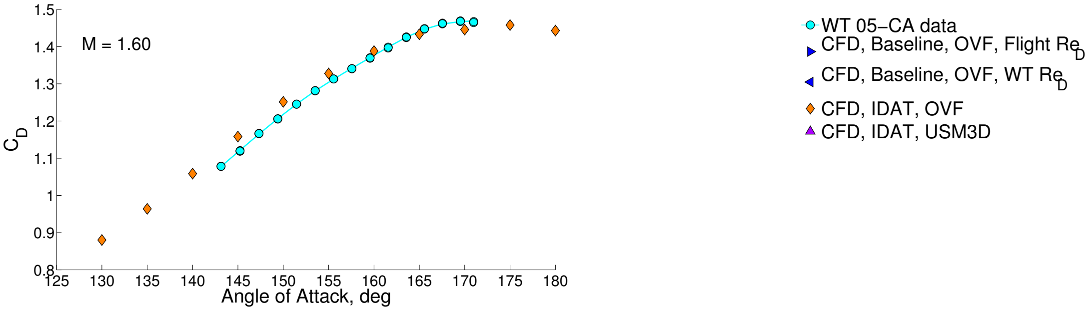

(e) $M_\infty = 1.6$ (f) Legend.

Figure 9: Drag Coefficient vs. angle of attack for available experimental and computational data for $\alpha > 130°$ at a range of Mach numbers, $M_\infty = 0.3$ to 1.6.

Transonic Facility is planned to provide flight Reynolds number data for $M_\infty \leq 0.9$.

As a result of the difficulties with the CFD solutions, the database nominals for $M_\infty < 1.5$ are developed where possible from the wind tunnel data only. The CFD data is used heavily in the uncertainty development and for the nominals outside of the $140° \leq M_\infty \leq 172°$ range.

III. Nominal Coefficient Development

The nominal coefficients for the database have been developed by smoothing and merging the available data sets at the cardinal database Mach numbers (M) using curve fitting techniques implemented in MATLAB®.[39] More advanced response surface and data fusion methodologies were not used initially in order to focus on the data quality issues at the subsonic Mach numbers. This simple methodology was then expanded to include breakpoints for $M \leq 8$. It is anticipated that the more advanced methods will be implemented in the next database update.

The basic smoothing and blending techniques common to the development are described first. Then the nominal development discussion is grouped according to the methodologies applied to each block of Mach numbers. The smoothing and blending techiques have been applied and adjusted to suit the available data in a given database space. The experimental data dominant block covers the Mach numbers below 1.4 where both WT and CFD data is available. Here, the WT data is used exclusively for the range of angles attack where it is available, and blended to the CFD data outside of this range. In the CFD + WT combined block, $1.6 \leq M \leq 4$, the WT and CFD data are combined over the WT angle-of-attack range. There are three Mach numbers ($M = 0.6$, 0.8, 1.4) where experimental data are available that were not originally cardinal Mach numbers in the database, and no CFD has been run at these conditions. The WT data suggested that the trends in Mach number were not linear between the existing cardinal Mach numbers, and database breakpoints were developed in this WT + interpolated CFD block. The nominals for $M = 6$ are developed with the CFD and WT data combined for $\alpha > 140°$, but only use the CFD for $\alpha < 140°$ so as to better capture the effects of the wider IDAT backshell angle. The last set of nominals is for $M = 8.0$. These combine the aerothermal CFD to the primary set of OVERFLOW CFD data in a similar manner as for the $1.6 \leq M \leq 4$ conditions.

III.A. Smoothing and Curve Fitting Methodologies

The basic process for developing the nominal coefficients for the database was to develop smooth data sets for the experimental and CFD data separately. The two sets were then combined according to how each set was to be used within a particular Mach number range.

The general smoothing approach uses the `‘SmoothingSpline’` type of fit from the MATLAB® curve fitting toolbox.[39] The methodology provides one tuneable parameter, the `smoothing factor` (sf). This relaxation parameter controls the degree to which the data is forced toward individual data points and can vary between 0 and 1. A value of 1 should force the curve to go through all data points, while small numbers produce a looser fitting curve. For smoothing both the CFD and experimental data, sf was set to 0.1, unless otherwise noted. For combining the CFD and WT data, sf was set to 0.01 unless otherwise noted.

The data for each of the four CFD data sets were separately smoothed in angle-of-attack into single curves for each for each coefficient (C_D, C_L, $C_{m_{cgx}}$) at each Mach number, defined at 1° increments over the full angle-of-attack range. For the 05-CA and 03-CA experimental data, the smoothing approach was used to combine runs where repeat run data were available, and to provide a smooth curve with the desired 1° increment in angle-of-attack. Note that the experimental data was only available over the angle of attack range of $142° \leq \alpha \leq 170°$. The data from the Mach 6 test (09-CA) was handled differently[d]. The highest Reynolds number runs were selected for each Mach number, and points at similar angles of attack were grouped, The angle of attack, C_D, C_L, and $C_{m_{cgx}}$ were averaged for each group, and then C_N, C_A, C_m, $C_{m_{cg}}$ and L/D were computed from the averaged data. Sample smoothed curves for both CFD and WT data are shown in Figure 10, for $M_\infty = 0.5$, along with the averaged data for Mach 6. The smoothed data CFD and WT sets were then combined to form the nominal coefficient data at each Mach number, and further manipulated for $\alpha < 120°$ to return the nominal curve to the averaged CFD data, rather than the smoothed. These steps are described in more detail in the next sections.

---

[d] The 09-CA data had been merged into a single set for the database much earlier in the project, and this merged set was used herein rather than the smoothing approach used for the lower speed tests.

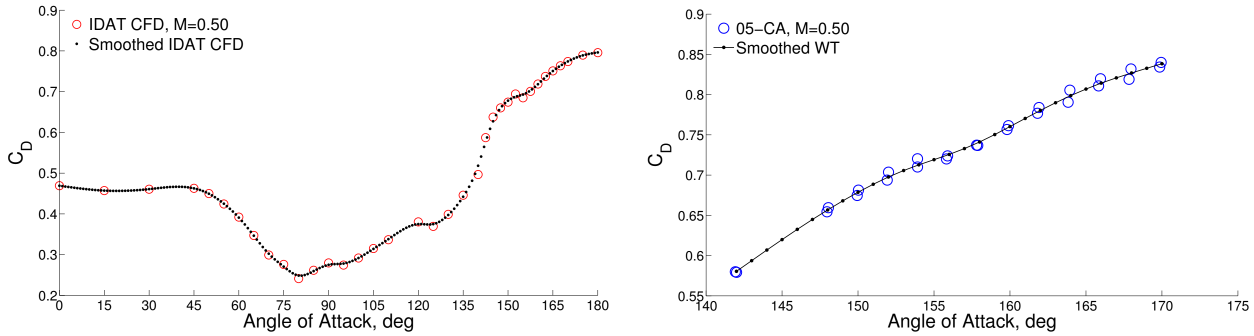

(a) Smoothed CFD curve, full angle-of-attack range

(b) Smoothed WT curve

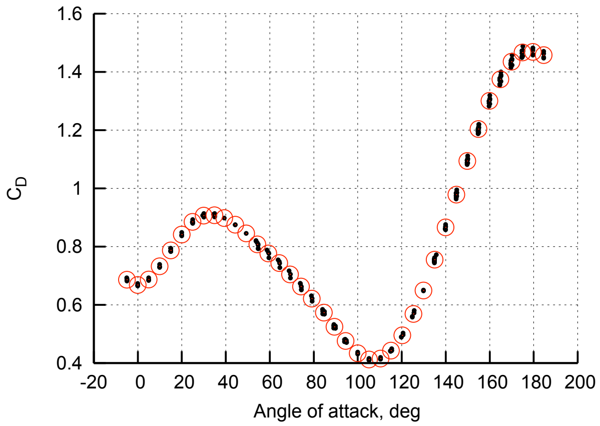

(c) Smoothed Mach 6 WT data, full angle-of-attack range

Figure 10: Examples of smoothing process for CFD and WT data sets.

III.B. Experimental data dominant, $M = \{0.3, 0.5, 0.7, 0.9, 0.95, 1.05, 1.1, 1.2\}$

For the subsonic and transonic Mach numbers, wind tunnel data was used exclusively where available because of the large variations seen in the CFD solutions in this region and the low drag overall predicted by the CFD, as discussed earlier. Before the smoothed WT and CFD data were combined for the final nominal curve, the CFD curve was modified to allow the WT data to dominate in the trim region. First, the data points in the range $142° \leq \alpha < 170°$ were removed. Adjustments to the CFD curve were then made for the range of $170° \leq \alpha \leq 180°$. For C_D and C_A, the CFD curve (for $\alpha \geq 170°$) was anchored to the WT curve at $\alpha = 170°$, so that the trend of the CFD data was used to fill in to 180°. For C_L, C_N, and C_m, the CFD curve was retained, with the coefficient value forced to zero at $\alpha = 180°$ so that the final curve would honor symmetry conditions at $\alpha = 180°$. For all coefficients, points for $171° \leq \alpha \leq 178°$ and $130° \leq \alpha < 142°$ were then removed, so that the smoothing process could better handle the transition between CFD to WT data. For $\alpha \leq 120°$, the CFD curve described in the previous section was retained. The smoothed WT curve and the modified CFD curve were then combined into a final nominal curve using the MATLAB® 'smoothing spline' with the sf set to 0.01. Figure 11 graphically shows this process. The points shown for the smoothed WT (blue circles) and modified CFD (red diamonds) are the data that are used to produce the combined curve (black).

To finalize the nominal curve, point density of the blended curve is reduced to match the database table breakpoints in angle-of-attack (every 5° between $0° \leq \alpha \leq 130°$ and every 2° between $130° \leq \alpha \leq 180°$) Additionally, the data for $\alpha \leq 120°$ was replaced by the original averaged CFD data. When there was not a data point at a specific database angle of attack (5°, 10°, etc.), the value from the smoothing process was retained.

Figure 12 shows the original WT and CFD data, the combined curve developed from the modified CFD curve, and the final nominal curve for C_D and C_L for the $M = 0.5$ condition. The effect of both the reduced density in the curve definition and replacement with the original CFD data is particularly noticeable at the

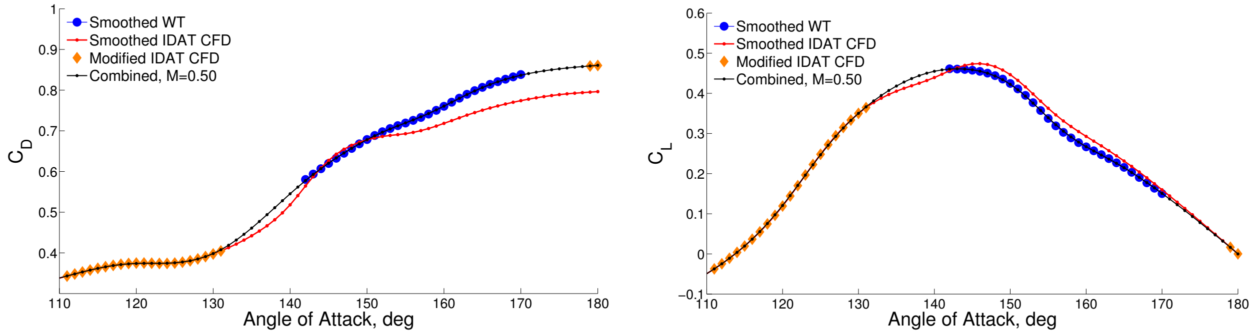

(a) C_D (b) C_L

Figure 11: Blending of WT and CFD, where WT data are dominant, $M = 0.5$

lowest Mach numbers near $\alpha = 60°$ where there is a steep gradient the C_L (and $C_{m_{cg}}$, not shown) data, Figure 12(b).

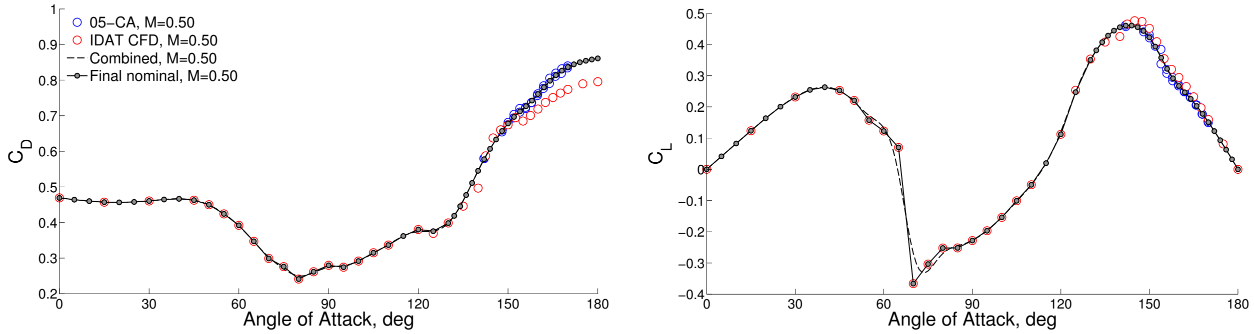

(a) C_D (b) C_L

Figure 12: Final nominal curve over full angle-of-attack range for $M = 0.5$

III.C. CFD + WT Combined, $M = \{1.6, 2.0, 2.5, 3.0, 4.0\}$

For the database breakpoints from $M = 1.6$ to $M = 4.0$, the experimental and CFD data are combined equally, as discussed in Section II.H. Note that the WT data was developed for the baseline geometry, and the CFD for the IDAT geometry. There are very limited CFD comparisons that suggest there is minimal difference in the aerodynamics for the baseline and IDAT geometries for $M_\infty > 1.6$ in the WT angle-of-attack range, and so the influence of the WT data is maintained. The process used is similar to that for the WT data dominant described in the previous section, except that the smoothed CFD data is retained over the angle-of-attack range where there is WT data. The CFD curve is still modified by deleting data between $130° \leq \alpha < 142°$ to facilitate blending. The CFD curve is again anchored (for C_A, C_D) at 170°, this time to the average of the WT and CFD data, and then the points for $171° \leq \alpha \leq 178°$ removed from the CFD curve. The modified CFD curve and the smoothed WT data are then combined using the MatLab® smoothing process to provide the final nominal curve. As with the previous process, the CFD smoothed curve is replaced with the averaged data for $\alpha < 120°$ when the curve is coarsened for the final database curve. Figure 13 graphically shows this process.

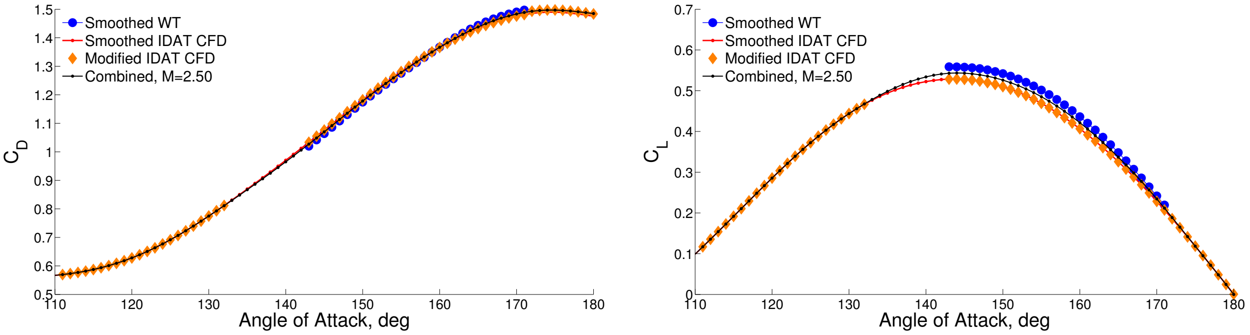

(a) C_D (b) C_L

Figure 13: Blending of WT and CFD, where WT and CFD data are combined equally, $M = 2.5$

III.D. WT + Interpolated CFD, $M = 0.6$, 0.8, 1.4

In versions of the aerodatabase prior to the most recent, the CM database tables included Mach number breakpoints at $M = \{0.3, 0.5, 0.7, 0.9, 0.95, 1.05, 1.1, 1.2, 1.6\}$, and CFD cases were typically run for these Mach numbers. The 05-CA WT data includes runs at $M_\infty = 0.6$, 0.8, 1.4 which were not previously incorporated into the database. Linear interpolation is used by the database between breakpoints, but the trends in the WT aerodynamic coefficients are not linear with Mach number. Figure 14 shows the variation in drag coefficient with Mach number for a range of angles of attack. The non-linearities are greatest between $M_\infty = 0.5$ and $M_\infty = 0.7$ for drag, and strongest between $M_\infty = 0.5$ and $M_\infty = 0.7$ for pitching moment[e].

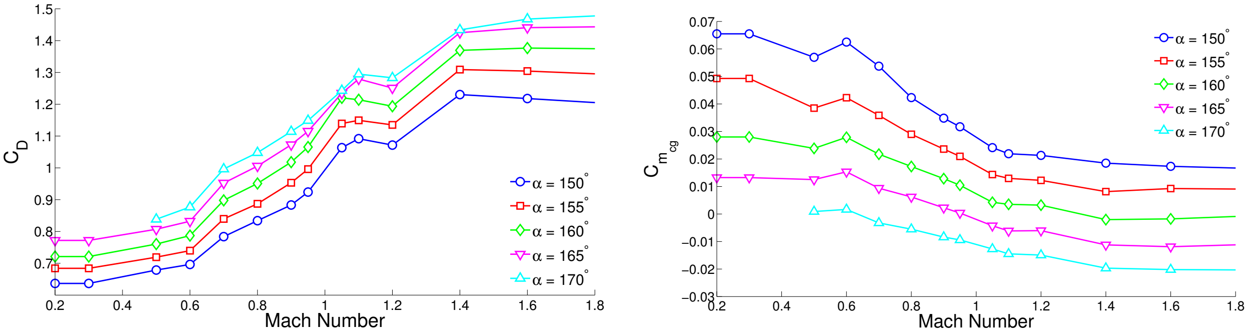

(a) C_D (b) $C_{m_{cgx}}$

Figure 14: C_D vs. Mach number for several angles of attack, smoothed 05-CA wind tunnel data.

To include these additional Mach number breakpoints in the database required creating a CFD curve by linearly interpolating in Mach number for each angle of attack between the surrounding available CFD curves, as shown in Figure 15 for $M = 1.6$. The interpolated CFD curve was then combined with the WT data in the same manner as was done for the $M \leq 1.2$ breakpoints, with the CFD ignored between $130° \leq \alpha \leq 178°$. Note that outside of the region where the wind tunnel data were available, no attempt at using the trends from the trim region was made; the current approach yields similar results as the linear interpolation used by the database when the additional breakpoints are not included. Figure 16 shows the final database curve for $M = 0.6$ plotted with both the WT data at $M_\infty = 0.6$ and the CFD data for $M_\infty = 0.5, 0.7$ for $\alpha > 110°$.

---

[e] Murphy et. al.[10] includes thorough discussion of Mach effects.

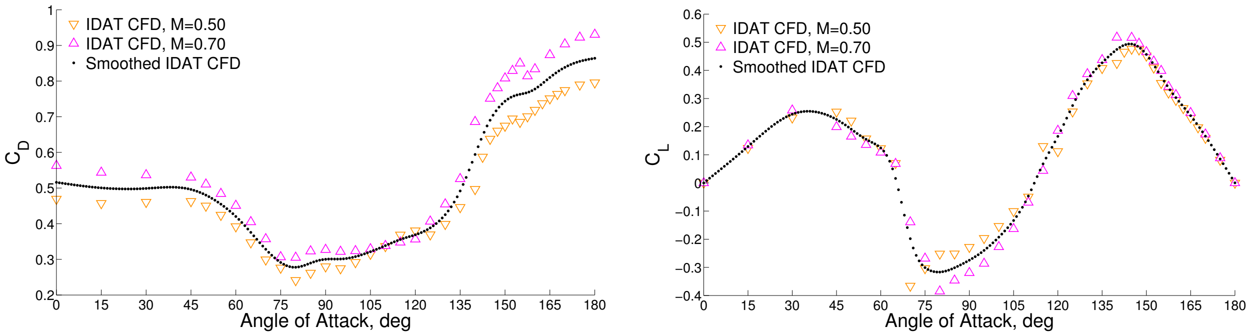

(a) C_D (b) C_L

Figure 15: Examples of combining CFD at nearby Mach numbers to get $M = 0.6$ CFD curve

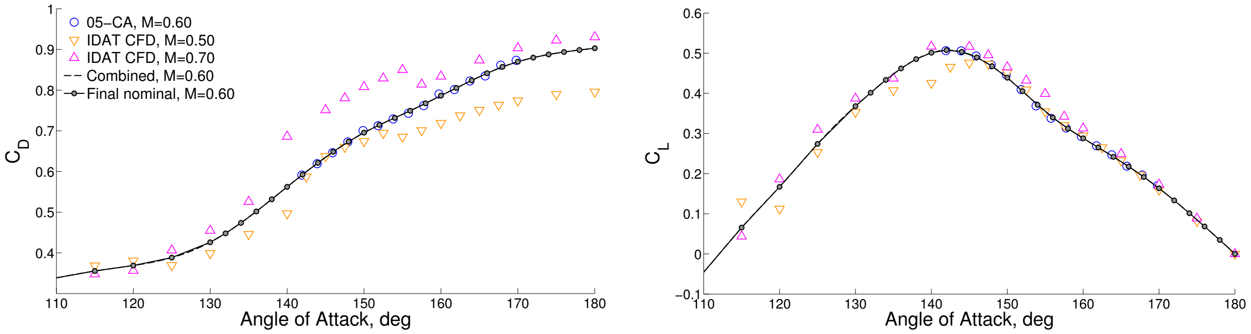

(a) C_D (b) C_L

Figure 16: Examples of combining interpolated CFD with WT to get final $M = 0.6$ nominal curve.

III.E. Hypersonic and Blending with WT, Mach 6

Both WT and CFD are available for the full angle-of-attack range for $M = 6$. However, since the wider backshell angle for the IDAT geometry would be expected to influence the aerodynamics for $\alpha < 140°$, the WT data is only used for $\alpha > 140°$. The full CFD curve is combined directly with the WT curve for $\alpha > 140°$. No anchoring is required since the angle-of-attack range for the WT data extends fully to 180°, and no modification of the CFD curve is necessary to ensure smooth blending because the two data sets are very close near $\alpha = 140°$. Figure 17 shows the blending for C_D and C_L. The available aerothermal data was not used to develop the nominal curve, but it is centered around the nominal curve.

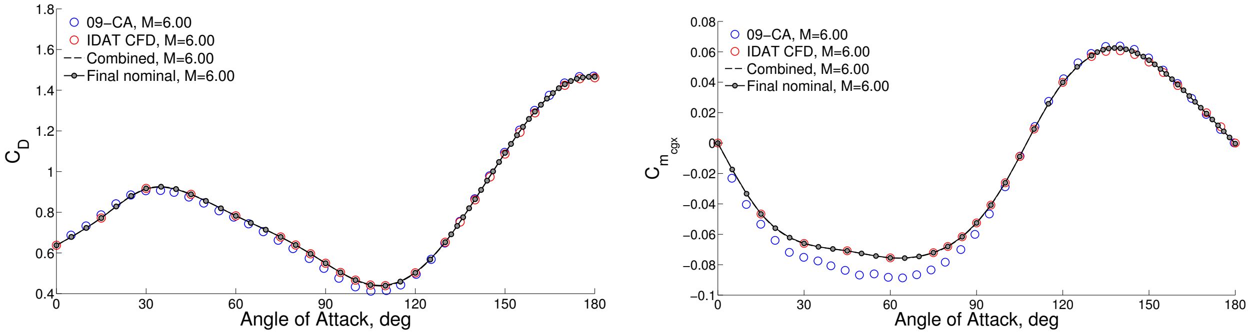

(a) C_D, M_∞ =6.0 (b) $C_{m_{cg}}$

Figure 17: Blending IDAT CFD with 09-CA data, $M = 6$

III.F. Blending with Aerothermal Data Set, $M = 8$

At $M = 8$, only CFD data is available. In addition to the primary Overflow set and the Usm3d set that cover the full angle-of-attack range, there is the aerothermal data set available in the trim range. Since this aerodatabase breakpoint is the border between the two database development methodologies, the aerothermal data set is incorporated into the nominal. This is accomplished using the same methodology as was used for the subsonic data, with the aerothermal data treated like the WT data and the blending occurring in the same manner.

Figure 18 shows the Overflow IDAT CFD data, the available aerothermal data, and the final nominal curve for C_D and C_L over the trim angle-of-attack range. The drag shows a noticeable effect of the real gas air chemistry used for the aerothermal data set. This effect of the real gas chemistry is incorporated into the uncertainty model, as described in a later section.

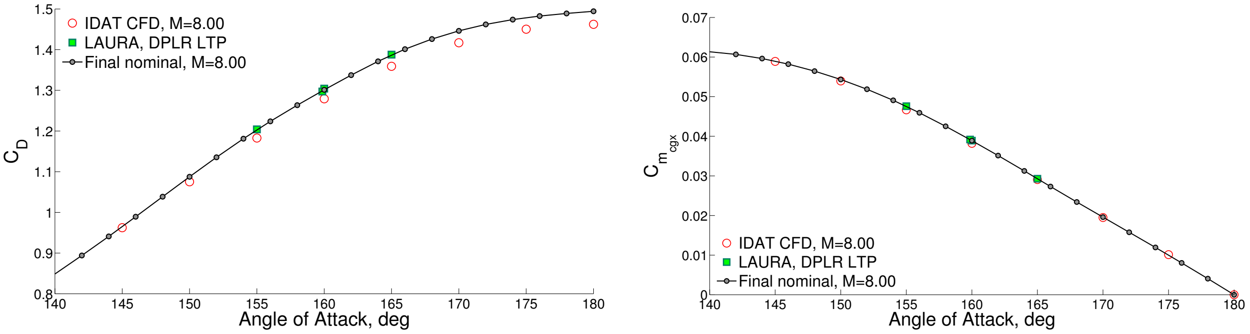

(a) C_D

(b) $C_{m_{cgx}}$

Figure 18: Final nominal aerodynamics compared to available data for $M = 8$, $\alpha > 140°$.

IV. Uncertainty Development

The uncertainty buildup followed the general methodology being employed by CAP.[40–45] Individual contributions are combined with either an RSS or additive method. The final buildup equation for the subsonic uncertainties is given as

$$UC_x = \delta_{Re} + MI_{hs}\ MI_{idat}\ MI\ k\sqrt{(\sigma_{wt2cfd})^2 + (max(\sigma_{wt}, \sigma_{cfd}))^2 + (\sigma_{interp})^2}, \qquad (M < 1). \tag{2}$$

The formulation changes somewhat above Mach 1 to reflect the different data used in the nominal development, such that

$$UC_x = \delta_{ltp} + \delta_{alt} + \delta_{chem} + \delta_{hs} + MI_{idat}\ MI\ k\sqrt{(\sigma_{wt2cfd})^2 + (max(\sigma_{wt}, \sigma_{cfd}))^2 + (\sigma_{interp})^2}, \qquad (M > 1). \tag{3}$$

The terms under the square root represent the variations seen in the data for common conditions, and include wind tunnel measurement/repeatability uncertainties, variations in CFD solutions, wind tunnel to CFD variations, and data interpolation uncertainties. These terms are combined with a root sum square (RSS) because they are assumed to be independent of one another (i.e. uncorrelated). They are developed based using range-based standard deviations that are modeled across the FMV-α_T space, as described in detail in the companion paper[7] for the development of the σ_{ltp} term.

Terms that are additive (e.g. δ_{Re}) represent a range that is covered by the database, such as the range of Reynolds numbers seen in flight. These terms are similar to the variation terms, but are based on ranges of data rather than standard deviations.

The various margin index (MI) terms are applied to the RSS term to cover unquantified variations such as subsonic heatshield asymmetry MI_{hs}, the variation due to the change in backshell angle MI_{idat}, and a general term covering unknown unknowns. The MI also provides coverage for lack of data. It does not cover large deviations from the current geometry. The development of each of the terms is covered below.

IV.A. Variation terms, RSS

The terms in the uncertainty buildup that are combined with a root-sum-square, RSS, method are standard deviation terms for the specified variation and are expressed as,

$$RSS = \sqrt{(\sigma_{wt2cfd})^2 + (max(\sigma_{wt}, \sigma_{cfd}))^2 + (\sigma_{interp})^2}. \tag{4}$$

These terms are developed using a range-based formula for σ,

$$\sigma_i = \overline{R_i}/d_2, \tag{5}$$

where d_2 is a bias correction factor for converting range to standard deviation, based on sample size.[42] The collection of σ_i values for a particular term are analyzed, and a model, $\sigma_{()}$, for the variation term is developed, typically as a function of M_∞, α. The model is then incorporated into the uncertainty buildup.

IV.A.1. Wind Tunnel Accuracy, σ_{wt}

The term for the wind tunnel accuracy, σ_{wt}, combines a term for repeatability and reproducibility[f] ($\sigma_{wt_{RR}}$) and balance accuracy ($\sigma_{wt_{bal}}$),

$$\sigma_{wt} = \sqrt{(\sigma_{wt_{RR}})^2 + (\sigma_{wt_{bal}})^2}. \tag{6}$$

The balance accuracy term was developed from balance calibration data provided by the Ames Balance Calibration Lab[46] for the MK13A task balance used in the `05-CA` test. The 1-σ error values provided in Ref. 46 were transformed into the force and moment accuracies using the methodology for force type balances described by Ulbrich.[47] The accuracies were then converted to coefficient form using the dynamic pressure for representative runs at each Mach number. Similar methodology was used for the `03-CA` and `09-CA` tests.

The repeatability term is developed as a function of (M_∞, α) based on the repeat run data from the various wind tunnel tests. For the `05-CA` and `03-CA` wind tunnel tests, the reported repeatability was a single set of values covering the entire test range. The data from these tests were re-analyzed to produce a model that better reflected trends, particularly in Mach number, for the test-to-test repeatability. The repeatability term for $M = 6$ was taken directly from the `09-CA` report.[11]

Development of the repeatability term started with Chan's MATLAB® repeat run analysis process[48] to compute the individual σ_{RR_i} values for the cardinal angles of attack for the test at each Mach number. Only repeat data for the high Reynolds number data used in the nominal coefficient data was included in this analysis. Figure 19 shows these values plotted vs. both Mach number and angle of attack, for drag and pitching moment. The repeatability improves greatly for supersonic Mach numbers; this change in character suggests separate modeling approaches for subsonic/transonic and supersonic Mach numbers. The `05-CA` data for above and below $M_\infty = 1.4$ were acquired in separate test sections of the Ames UPWT facility; the split in the modeling approach for the repeatability is therefore made between the $M = 1.4$ and $M = 1.6$ database breakpoints. Trends in angle-of-attack in the σ_{RR_i} data are evident for pitching moment (and lift, not shown) but not for drag with all of the data pooled as in Figure 19.

For the subsonic to low supersonic data from the `05-CA` test in the 11x11 leg of AUPWT, a multivariate regression within MATLAB® was used to fit the variations to a model that gives σ_{RR} as an $f(M_\infty, \alpha)$. This approach allows the model to capture trends in both Mach number and angle-of-attack and provide repeatability data at the Mach numbers where there is not any available (e.g., $M_\infty = 0.6, 0.9$). Figure 20 shows the σ_{RR} model (blue diamonds) and the associated coverage, $k\sigma_{RR}$, compared with the $M_\infty = 0.50$ `05-CA` repeat data. The average of the σ_{RR_i} data at the current Mach number is shown by the red line. Generally, the multivariate model provides a better description of the repeat data than the average. The blue line, $k\sigma_{RR}$, is the coverage level for the uncertainty term, and should cover most of the data.

For $M_\infty \geq 1.4$, the average of the σ_{RR_i} data at each Mach number was used. Because there were no significant trends with angle-of-attack, and the values for σ_{RR_avg} provided a reasonable representation of the σ_{RR_i} data, this simpler approach was chosen. For $M_\infty = 2.0$, where there was no repeat data available, $\sigma_{RR_{avg}}$ for $M_\infty = 1.6$ was used. For the Mach 6 test, the reported repeat run data[11] was used directly.

---

[f] This term is ultimately derived using multiple levels of variation, representative of the dominate level of variation, and not limited to short-term measures of repeatability.

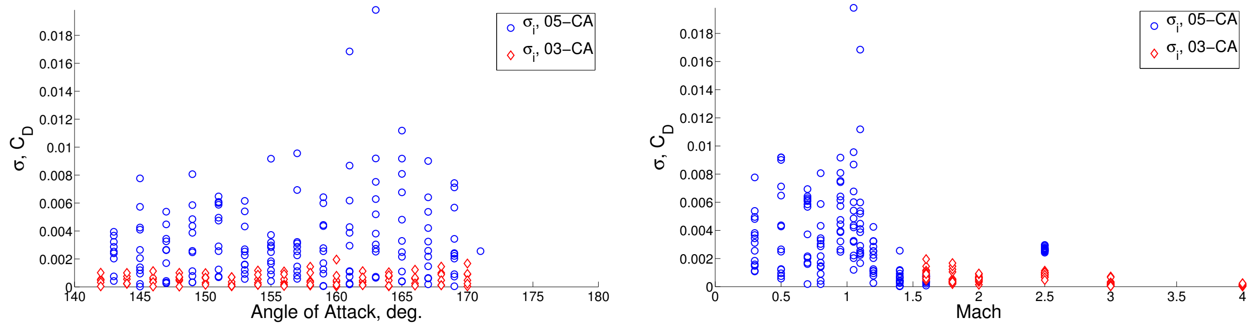

(a) Drag variation vs. angle of attack

(b) Drag variation vs. Mach number

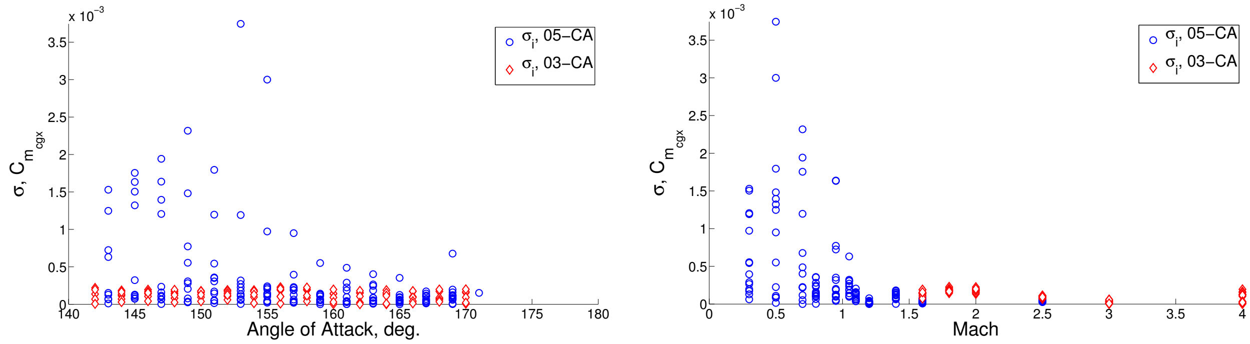

(c) Pitching-moment variation vs. angle of attack

(d) Pitching-moment variation vs. Mach number

Figure 19: Wind tunnel repeatability range-based standard deviation data for the 05-CA and 03-CA tests.

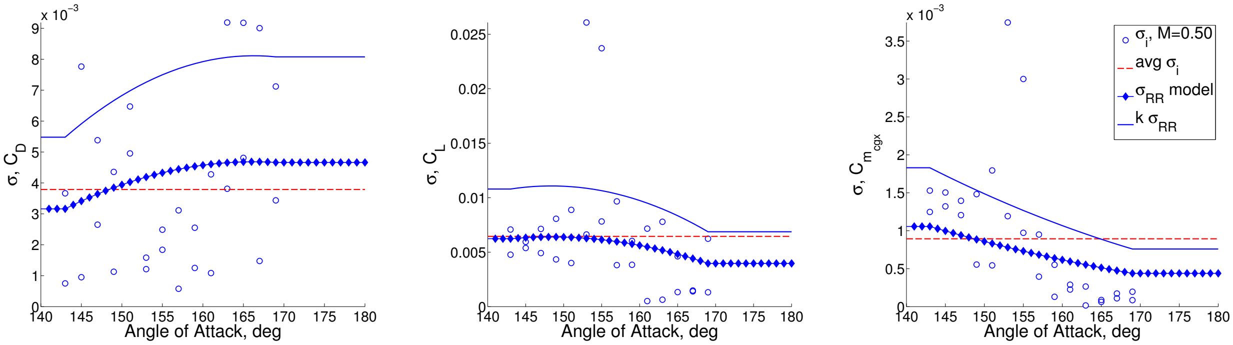

(a) C_D

(b) C_L

(c) $C_{m_{cg}}$

Figure 20: Development of model for σ_{RR} as an $f(M_\infty, \alpha)$, for C_D, C_L, and C_m at $M = 0.50$.

Sample buildups for the full wind tunnel accuracy term (Eqn. 6) are shown in Figure 21 for C_D, C_L and C_m at $M = 0.5$ and $M = 2.5$. The green line with symbols gives the balance accuracy term, $\sigma_{wt_{bal}}$. The curve used for $\sigma_{wt_{RR}}$ from the previous plot set is again shown with blue diamonds in the uncertainty buildup. The red squares show the RSS of the two terms; this is the term that is used in the final uncertainty buildup for σ_{wt}. In general, the wind tunnel accuracy term is dominated by the run-to-run repeatability.

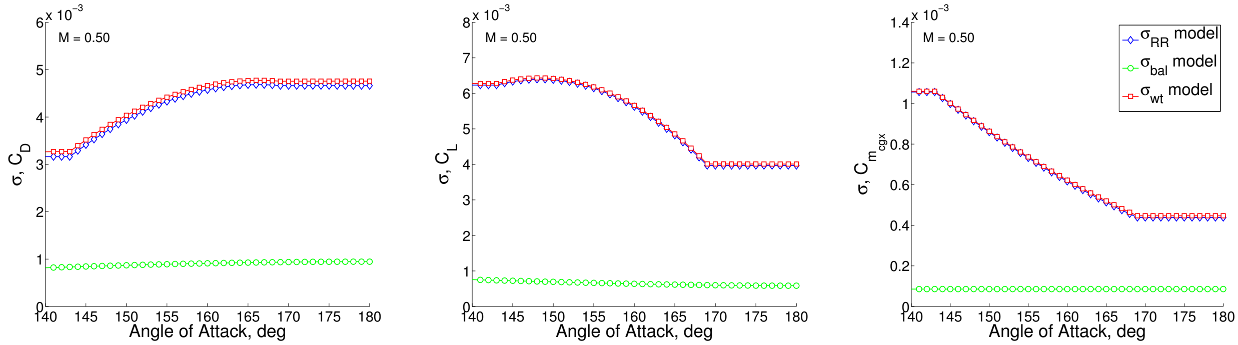

(a) C_D, $M = 0.50$ (b) C_L, $M = 0.50$ (c) $C_{m_{cgx}}$, $M = 0.50$

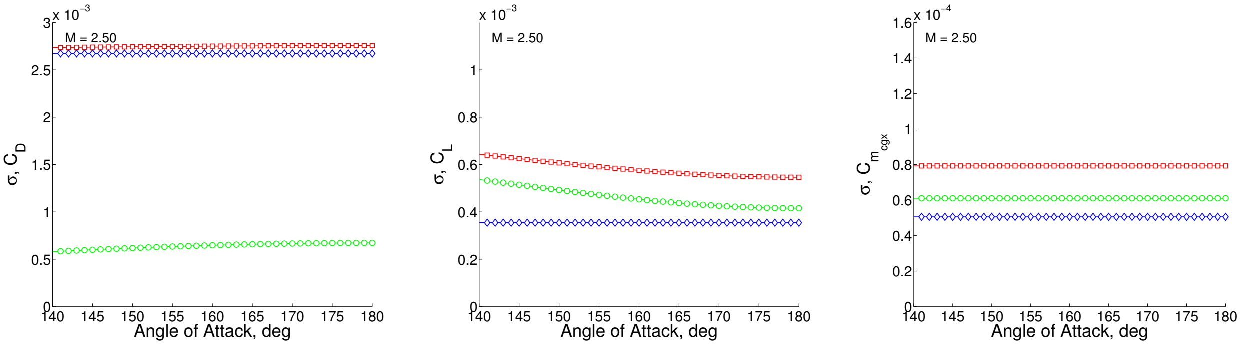

(d) C_D, $M = 2.50$ (e) C_L, $M = 2.50$ (f) $C_{m_{cgx}}$, $M = 2.50$

Figure 21: Example wind tunnel accuracy buildup, for C_D. C_L and C_m at two Mach numbers.

IV.A.2. CFD Accuracy, $\boldsymbol{\sigma_{cfd}}$

The CFD accuracy term, Equation 7, combines a repeatability term, $\sigma_{ovf_{RR}}$, for the OVERFLOW computations with a term, σ_{c2c}, representing differences between OVERFLOW and USM3D at common conditions.

$$\sigma_{cfd} = \sqrt{(\sigma_{ovf_{RR}})^2 + (\sigma_{c2c})^2} \tag{7}$$

The set of OVERFLOW solutions on the nominal backshell geometry had considerable duplication, with the differences between cases including the CFD analyst and minor code and grid inputs. While these solutions should be nearly identical, they were not. Their variation was used to develop a repeatability term for CFD in a similar manner as the wind tunnel repeatability term,

$$\sigma_{ovf_{RRi}} = \frac{\left| C_{x_{max}} - C_{x_{min}} \right|}{d_2}. \tag{8}$$

There were either 2 or 3 CFD solutions available for each condition, and the repeats were only at M_∞ = 0.3, 0.5, 0.7, and 0.9. The model for $\sigma_{ovf_{RR}}$ was developed at these Mach numbers, and extended to smoothly cover the full subsonic range, up to $M = 0.95$. Figure 22 shows the repeat term for $M = 0.5$. The largest differences occurred in regions where the coefficients were changing more rapidly with angle of attack, particularly near $\alpha = 60°$ and $\alpha = 155°$.

The second term, σ_{c2c}, was developed at $M = 0.5$, 1.2, 2.5, and 8.0 for the full angle-of-attack range, with the individual variation terms computed as

$$\sigma_{ovf_{usmi}} = \frac{\left| C_{x_{ovf}} - C_{x_{usm}} \right|}{d_2}. \tag{9}$$

Some USM3D data was available for M_∞ =0.7, 0.9, and 0.95 in the trim angle-of-attack range, but was not used in the uncertainty development. This data had been largely discounted due to previously described

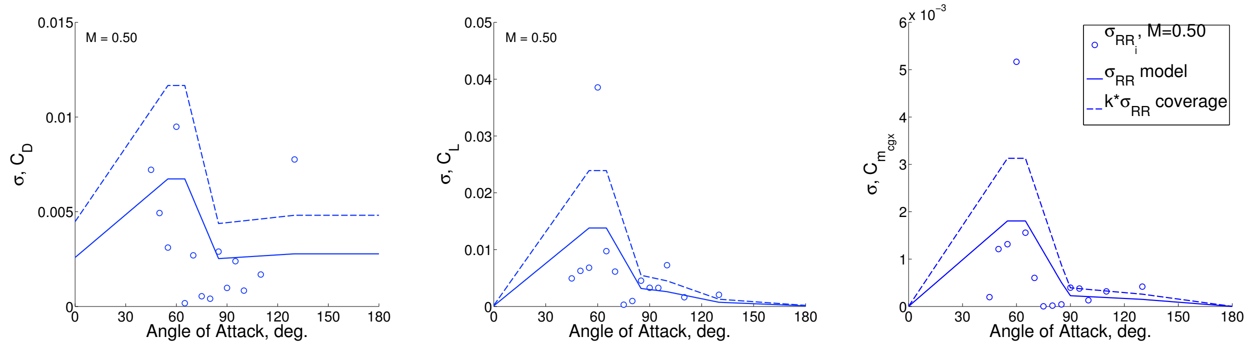

(a) C_D (b) C_L (c) $C_{m_{cg}}$

Figure 22: Development of model for $\sigma_{ovf_{RR}}$ as an $f(\alpha)$, for C_D, C_L, and $C_{m_{cg}}$ at $M = 0.50$.

problems with the subsonic trim CFD data in general, and because the CFD data was not used for nominal coefficient development in this angle-of-attack range below $M = 1.6$. Figure 23 shows the code-to-code comparison for $M = 0.5$. Note that the data around $\alpha = 150°$ is ignored in the model for σ_{c2c}.

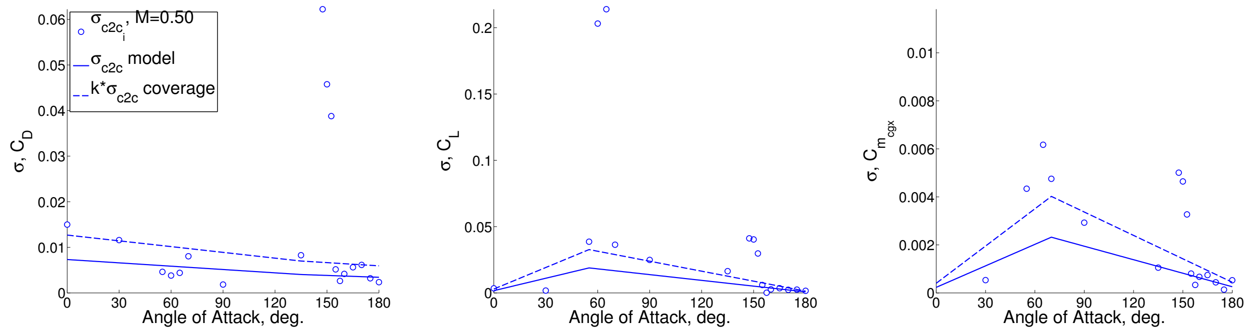

(a) C_D (b) C_L (c) $C_{m_{cg}}$

Figure 23: Development of model for σ_{c2c} as an $f(\alpha)$, for C_D, C_L, and C_m at $M = 0.50$.

Other options for the σ_{cfd} term were explored. Using the CFD iterative convergence criteria was not deemed appropriate. While the minimal convergence criteria was consistent for all CFD solutions, it was typically exceeded greatly for steady flow solutions. For unsteady flow solutions, where the coefficients were averaged over time, the convergence criteria was not a relevant parameter. Grid convergence levels were also difficult to use, primarily because the appropriate values were not readily available for the current CFD.

IV.A.3. Wind Tunnel - CFD Variations, σ_{wt2cfd}

For the subsonic Mach numbers, there is sufficient data to develop a term that compares the wind tunnel data to CFD data at wind tunnel conditions. This term is developed as Equation 10:

$$\sigma_{wt2cfd_i} = \frac{\left| C_{x_{wt}} - C_{x_{cfd_{wtRe}}} \right|}{d_2}, \qquad (M < 1). \tag{10}$$

The model for this term is shown in Figure 24 for $M = 0.5$. Final modeling of this term (subsonically) was problematic due to the large jumps in the CFD data around $\alpha = 150$, and the fact that this data was not used in the nominal development. This term was kept in the buildup, however, to provide some recognition that there are legitimate discrepancies between the WT and CFD data. The average value of σ_{wt2cfd_i} was used for the model, with some reduction near $\alpha = 0°, 180°$ to recognize symmetry conditions. This term, more than most, is developed with much engineering judgement.

For the higher Mach numbers, there is not a direct comparison between the wind tunnel data and CFD data at wind tunnel conditions. The only available CFD data is at flight conditions, and is on the IDAT

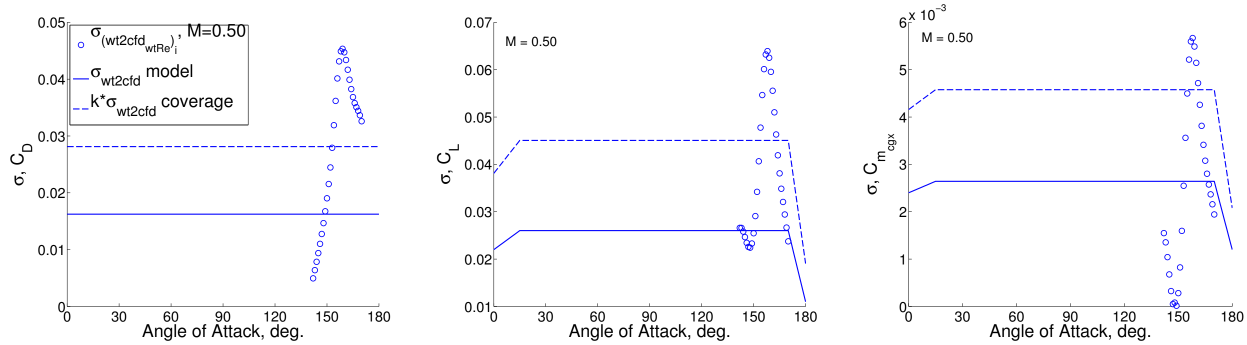

(a) C_D (b) C_L (c) $C_{m_{cg}}$

Figure 24: Development of model for σ_{wt2cfd} as an $f(\alpha)$, for C_D, C_L, and C_m at $M_\infty = 0.50$.

geometry. An approach is used which computes a term similar to Equation 10 using the available data,

$$\sigma_{wt2cfd_{flt_i}} = \frac{\left|C_{x_{wt}} - C_{x_{cfd_{flt,idat}}}\right|}{d_2}, \qquad (M > 1). \tag{11}$$

The altitude variation (which is comparable to Reynolds number variation at higher speeds) is then removed to provide a comparable term to the subsonic term,

$$\sigma_{wt2cfd} = \sqrt{\sigma^2_{wt2cfd_{flt}} - \sigma^2_{alt}}, \qquad (M > 1). \tag{12}$$

This term is small compared to the magnitude of the term for $M < 1$. The effect of the IDAT backshell is still buried in the σ_{wt2cfd} term. To compensate for this, $M\!\!I_{idat}$ is set to 1.0 for $M > 1.4$. For $1 < M \leq 1.4$, the estimated effect of the IDAT backshell is perhaps over counted.

IV.A.4. Interpolation Error

The term representing interpolation error, σ_{interp}, in Equations 2, 3, and 4, was not quantified for the CM database but included for completeness. Development of this term is problematic. Due to the lack of data that would be considered representative of the flight vehicle, interpolation error would have to be determined for each of the constitutive data sets and propagated into the final database definition. More importantly, interpolation error is expected to be negligible except for a small region well outside the flight envelope. For $\alpha > 130°$, the database point density in angle-of-attack is every $2°$, and should be sufficient to capture the smooth trends in this region with a negligible interpolation error. Outside of this range, $\alpha < 130°$, the point density every $5°$, but the trends are still smooth over most of the domain; the exception is where there are steep gradients around $\alpha = 60°$ for the lower subsonic Mach numbers. The interpolation error is ignored in the uncertainty buildup, such that

$$\sigma_{interp} \approx 0. \tag{13}$$

IV.B. Flight Condition Coverage Terms, δ_{Re}, δ_{alt}, δ_{ltp}, δ_{chem}

There are several terms in the uncertainty buildup that serve to cover flight conditions that are not characterized by Mach number or velocity. These terms could have been included as additional independent variables in the nominal database development, but were considered small enough to be covered instead by the uncertainties. These coverage terms are added to the uncertainty buildup, and are developed based on range data. For the subsonic Mach numbers, the primary additional variable is Reynolds number; the term δ_{Re} is developed from CFD solutions at the bounding Reynolds number conditions. Above Mach 1, the data is not available to provide a Reynolds number coverage term directly. Instead, the effect of altitude variation,δ_{alt}, developed from the aerothermal data set is used. As Mach number increases, the opportunity for laminar flow over the vehicle heatshield increases, and so the difference between fully laminar and fully turbulent flow are included as δ_{ltp}. Lastly, as Mach number increases, the effects of reacting gas chemistry on the aerodynamics begin to be noticed. The reacting air chemistry is not modeled by either the OVERFLOW or USM3D flow solvers, and so coverage for this effect, δ_{chem}, is developed using the aerothermal data set.

IV.B.1. Reynolds Number Coverage, δ_{Re}

The term in the uncertainty buildup for the subsonic Reynolds number increment, δ_{Re}, was developed using the WT and flight Reynolds number CFD and a run-to-run variation analysis. The difference between computations at WT and flight Reynolds numbers was computed as

$$\delta_{Re_i} = \frac{|C_{x_{flt}} - C_{x_{wtRe}}|}{2}. \tag{14}$$

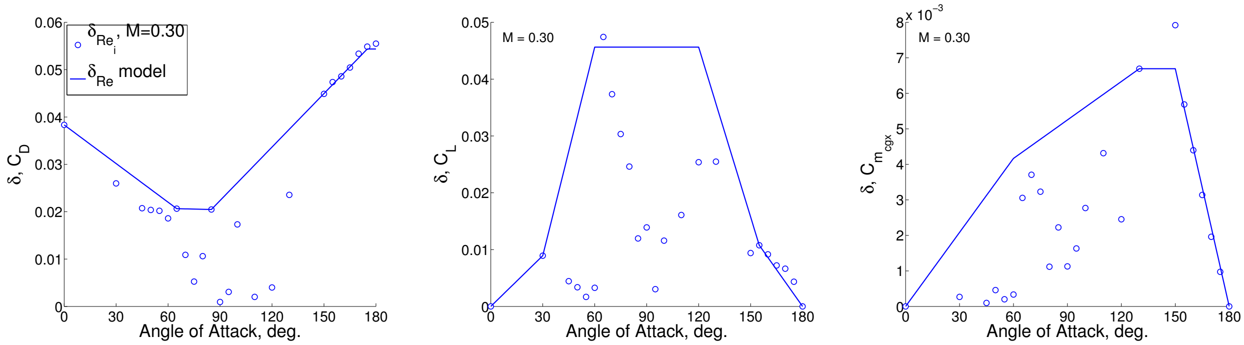

(a) C_D, $M = 0.30$ (b) C_L, $M = 0.30$ (c) $C_{m_{cgx}}$, $M = 0.30$

Figure 25: Development of δ_{Re}, for C_D, C_L, and $C_{m_{cgx}}$ at $M = 0.30$.

The computed values for δ_{Re_i} at $M = 0.3$ are shown in Figure 25. The model for δ_{Re} is shown by the line, and is developed by loosely following the trends of the δ_{Re_i} data. Although not shown here, the variation in Reynolds number decreases as Mach number increases. For drag, particularly at the lower Mach numbers, the Reynolds number effects are greatest near $\alpha = 0°$ and $\alpha = 180°$. This is consistent with the flow physics, with the largest wake sizes at these angles and the turbulent wake being very sensitive to Re_D. The lift and pitching moment, however, show an opposite trend with angle of attack, and the model for δ_{Re} is forced to zero for both C_L and $C_{m_{cg}}$ at $\alpha = 0°, 180°$ in order to preserve symmetry relations.

IV.B.2. Altitude Coverage, δ_{alt}

The altitude coverage term is developed in a similar manner as the σ_{alt} term in the hypersonic uncertainty buildup in the companion paper,[7] using all of the aerothermal data for $FMV < 9$. The range data for each group of *ltp* aerothermal data points at a single velocity and angle of attack and computed with a single CFD code are used directly without dividing by the d_2 factor, such that

$$\delta_{alt_i} = |C_{x_{max}} - C_{x_{min}}|. \tag{15}$$

Figure 26 shows the individual δ_{alt_i} values plotted vs. Mach number. Because there are not a large number of data points, the model for δ_{alt} is simply the average of all of the values. Note that the model drops to zero for subsonic Mach numbers.

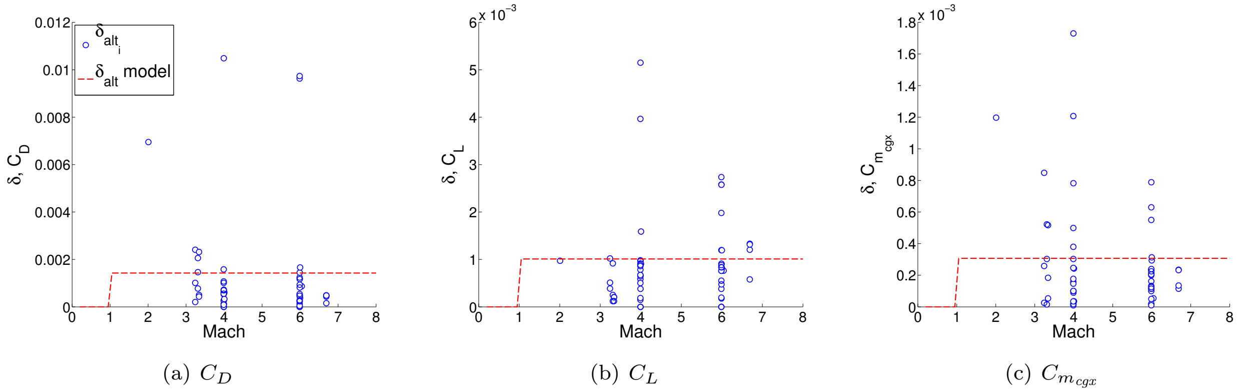

(a) C_D (b) C_L (c) $C_{m_{cgx}}$

Figure 26: Development of δ_{alt}, for C_D, C_L, and $C_{m_{cgx}}$.

IV.B.3. Laminar-Turbulent Coverage, δ_{ltp}

All of the CFD data from the OVERFLOW and USM3D data sets are fully turbulent. The aerothermal computations are run such that there is (usually) a laminar and turbulent solution for each condition, and these solutions generate slightly different aerodynamic forces and moments. For the hypersonic database development, a variation was computed to account for the notion that the true boundary layer state isn't known, and that the aerodynamics should be bounded by the laminar and fully turbulent solutions[g]. This term doesn't account for the possible effects of asymmetric transition. A similar term is computed here, using the range data as with the altitude term above, with

$$\delta_{ltp_i} = |C_{x_{lam}} - C_{x_{turb}}|. \tag{16}$$

Figure 27 shows the individual δ_{ltp_i} values plotted versus angle of attack. As with the altitude term, the average value is used for the final δ_{ltp} model. It is interesting to note that the highest angles of attack (around $\alpha = 172°$) show the most variation between laminar and turbulent. As more data becomes available, this trend may be modeled in the future.

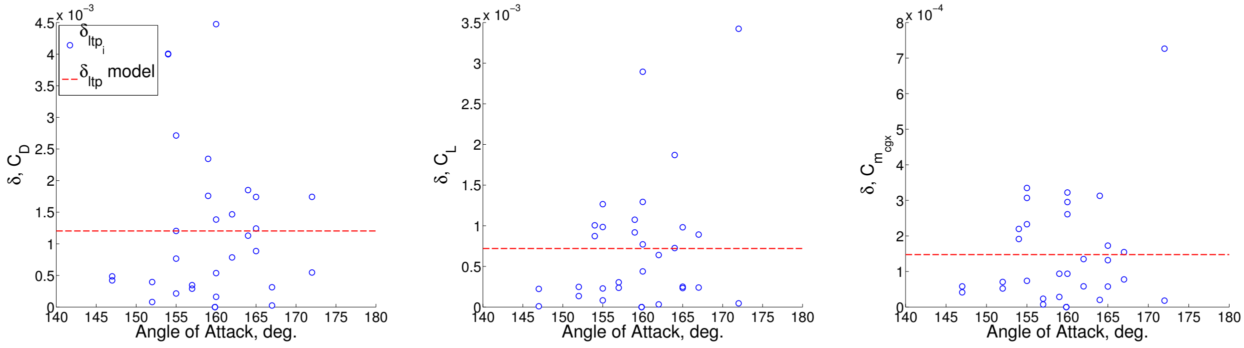

(a) C_D (b) C_L (c) $C_{m_{cgx}}$

Figure 27: Development of δ_{ltp}, for C_D, C_L, and $C_{m_{cgx}}$.

IV.B.4. Real Gas Chemistry Coverage, δ_{chem}

Above Mach 2, the vehicle can experience real gas chemistry effects in the aerodynamic forces and moments. The majority of the computational and wind tunnel data for $M < 8$ does not account for these effects. A limited group of computations within the aerothermal data set, using LAURA, compared 5-species air and perfect gas air models and were used to establish an uncertainty model to account for the use of perfect gas

---

[g] Note that the bounding assumption has not been validated.

chemistry in the majority of the $M < 8$ data. The differences for a single angle of attack at 3 velocities were computed as

$$\delta_{chem_i} = |C_{x_{5sp}} - C_{x_{pg}}|. \tag{17}$$

Figure 28 shows the δ_{chem_i} values. In general, the real gas variation increases with Mach number, as expected. The uncertainty model for δ_{chem} is simply the line connecting the δ_{chem_i} data, anchored at zero for $M = 2.0$. For pitching moment, both the variation for $C_{m_{cg}}$ and $C_{m_{cgx}}$ were examined, and the maximum value used for the δ_{chem} model.

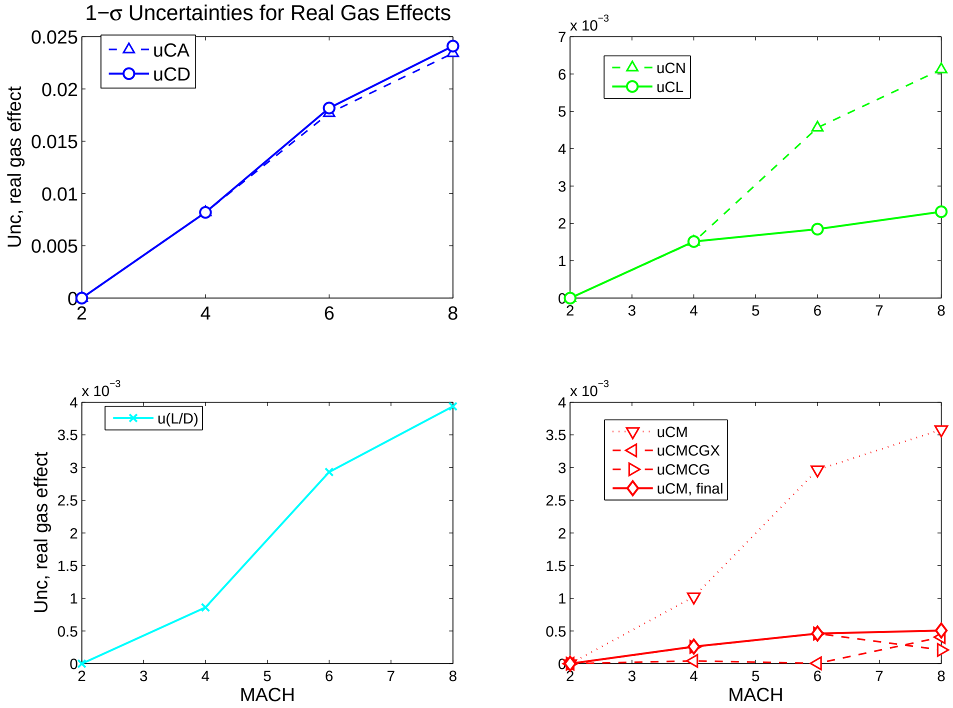

Figure 28: Uncertainties to cover real gas effects where not modeled.

IV.C. Geometry Variations

The database nominals have been developed from a mixture of smooth, axisymmetric geometries with different backshell angles. The effects of the backshell angle differences and heatshield asymmetries must be accounted for in the uncertainties where appropriate. The effects of other geometry variations such as the foot wells and windows have not been analyzed, and their effect is covered by the general margin index term, $M\!\!I$.

IV.C.1. IDAT Differences,

For angles of attack greater than 120°, where the database nominals were developed using data from the 32.5° backshell geometry, the difference due the change in backshell angle to 30° must be accounted for. For hypersonic Mach numbers, the companion paper showed neglible differences for $\alpha > 140°$; this trend should continue down to supersonic Mach numbers. While there were overlapping computations on both geometries for subsonic Mach numbers, extracting the difference in the solutions due solely to geometry proved difficult due to grid and CFD code execution differences. For a very limited number of cases, the difference was isolated, and found to be small. Because the differences were small, and only a few conditions available, a multiplier approach was used to cover differences where applicable. Equation 18 gives the values for MI_{idat} used in the uncertainty buildup.

$$\mathit{MI}_{idat} = \begin{cases} 1.0 & \text{if } \alpha \leq 120^\circ \\ \text{linear} & \text{if } 120^\circ < \alpha < 140^\circ \\ 1.1 & \text{if } \alpha \geq 140^\circ,\ M \leq 1.4 \\ 1.0 & \text{if } M > 1.4 \end{cases} \tag{18}$$

IV.C.2. Heatshield Asymmetry, $\mathit{MI}_{\mathrm{hs}}$, δ_{hs}

Only limited studies, primarily for hypersonic conditions, have been done to analyze the various asymmetric heatshield shapes. For a select few conditions, comparisons were made with Overflow at subsonic and supersonic Mach numbers; the geometry differences were again co-mingled with code and grid differences, and so those results could not be used directly. As a result, a factor, MI_{hs}, was applied to the RSS term in the uncertainty buildup for subsonic Mach numbers. The value of $\mathit{MI}_{hs} = 1.2$ is based loosely on the Overflow results. Above Mach 1.4, the heatshield coverage term δ_{hs} developed for the hypersonic portion of the database was applied. Details can be found in the companion paper.[7]

IV.D. Uncertainty Buildup for Longitudinal Aerodynamic Coefficients

Once all of the individual uncertainty terms are developed, they are collected according to Eqns. 2 and 3. The coverage factor remains $k = \sqrt{3}$ everywhere. The margin index factor, MI, is currently set as

$$\mathit{MI} = \begin{cases} 1.4 & \text{if } \alpha \leq 120^\circ \\ \text{linear} & \text{if } 120^\circ < \alpha < 140^\circ \\ 1.2 & \text{if } \alpha \geq 140^\circ \end{cases} \tag{19}$$

The larger margin for $\alpha < 120^\circ$ reflects the fact that the database nominals are developed entirely from CFD data in this region.

Figures 29–32 show the buildup of the database uncertainty for several Mach numbers, with the legend for all of these plots shown in Figure 29(c). The blue region at the bottom is the RSS term, with the light blue lines representing the components of the RSS term. The dark green shaded region is the Reynolds number coverage term that is applied for subsonic Mach numbers only. The various other coverage terms for $M > 1$ are shown in progressively lighter shades of green. The heatshield asymmetry term is in yellow, and represents either the δ_{hs} term for $M > 1$ or the MI_{hs} term subsonically. The IDAT coverage term is shown in orange, with the final MI contribution in dark red. Note that the various MI terms are formulated here as additive terms, so that the appropriate shaded region is $(\mathit{MI}_x - 1)\, RSS$.

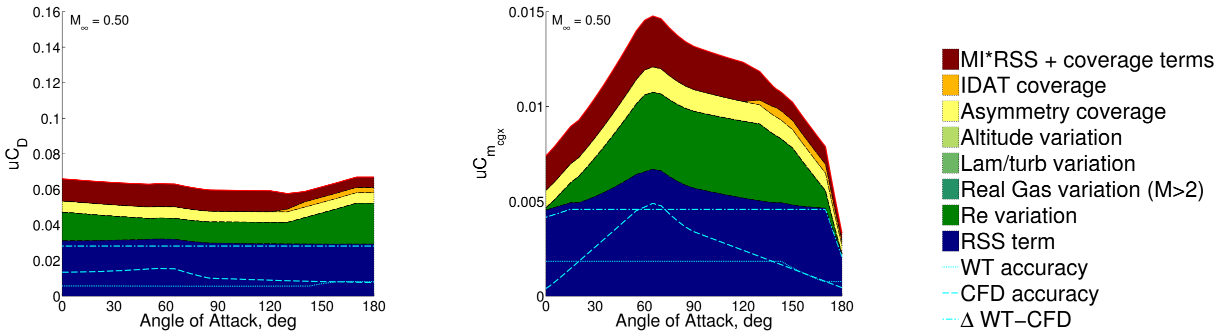

(a) C_D (b) $C_{m_{cgx}}$ (c) Legend

Figure 29: Uncertainty buildup, $M = 0.5$.

For subsonic Mach numbers, eg. $M = 0.5$ in Figure 29, the RSS term is dominated by the WT to CFD comparison term (dash-dot line), and is about half of the overall uncertainty. The Reynolds number coverage term (δ_{Re_D}, green shaded) is next in importance. Note that this term increases in the trim angle-of-attack region for drag. For uC_L and $uC_{m_{cg}}$, the uncertainty drops as α approaches 180°, due to the symmetry conditions discussed earlier. Note that uC_L is omitted in this figure to allow for the legend.

All of the uncertainties drop above Mach 1, primarily because Reynolds number effects are much smaller, as seen for $M = 1.1$ in Figure 30 The WT to CFD term still dominates the RSS portion of the uncertainties.

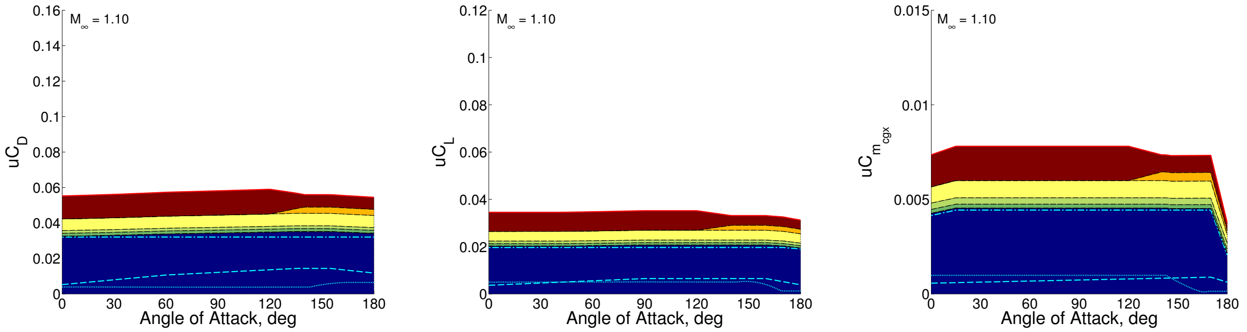

(a) C_D (b) C_L (c) $C_{m_{cgx}}$

Figure 30: Uncertainty buildup, $M = 1.1$, Legend in Figure 29(c)

At $M = 3$, Figure 31 the effect of the heatshield asymmetry term can be seen, and is roughly the same size as the RSS term. The real gas chemistry effects are also beginning to contribute, primarily to the drag uncertainty. For the highest Mach number, shown in Figure 32, the real gas chemistry effects dominate the drag uncertainty.

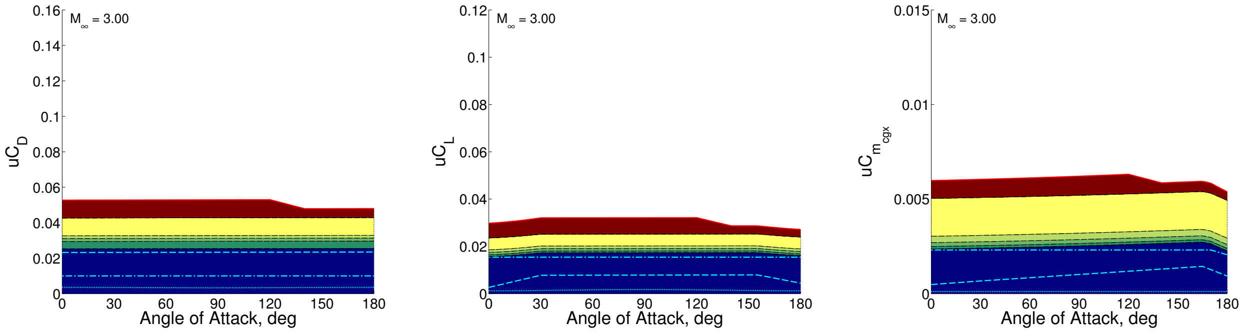

(a) C_D (b) C_L (c) $C_{m_{cgx}}$

Figure 31: Uncertainty buildup, $M = 3.0$, Legend in Figure 29(c)

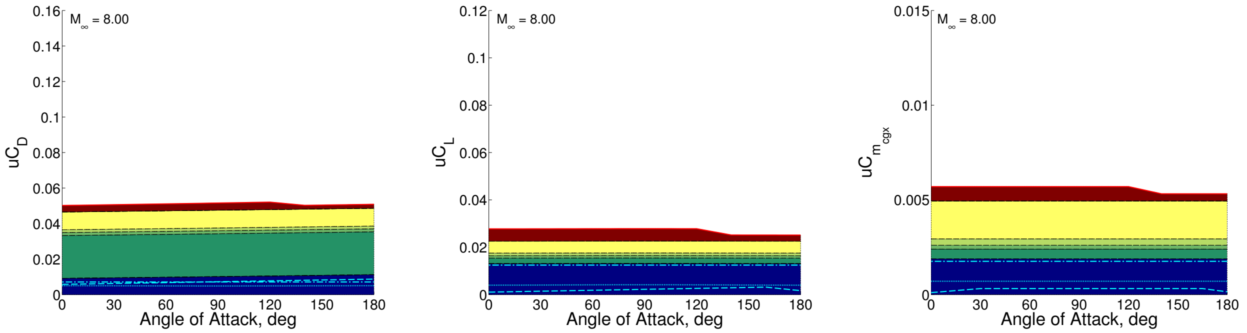

(a) C_D (b) C_L (c) $C_{m_{cgx}}$

Figure 32: Uncertainty buildup, $M = 8.0$, Legend in Figure 29(c)

Comparing the current uncertainties at $M = 8$ with the uncertainties from the companion paper[7] highlights the inconsistencies between the two approaches. Pitching moment uncertainties are comparable, drag uncertainties are lower for the hypersonic approach, and the lift uncertainties are lower for the current approach. These inconsistencies are a topic for further development for the Orion Aerodatabase.

IV.E. Lateral-Directional Uncertainties

The nominal and uncertainty development presented thus far has focused on the longitudinal aerodynamic coefficients. In reality, there is some finite level of uncertainty in the lateral-directional coefficients (C_y , C_n, and C_l). Developing these uncertainties is a challenge, as the majority of analysis is done for $\beta = 0°$ where these coefficients are either zero (for compuatational analyses), or smaller than balance uncertainties (in experimental data).

The lateral-directional nominal coefficients (C_y , C_n, C_l) are computed directly using the usual sine/cosine transformations based on axisymmetric assumptions, as described in the companion paper.[7] Side-force uncertainty is computed as

$$uC_Y = -uC_D \sin\beta, \tag{20}$$

Rolling moment uncertainty was set to $uC_l = 0.00005$ based on historical considerations, and has not been re-evaluated. The formulation of the yawing-moment uncertainty has evolved, and is briefly described below. The formulation for all of the lateral-directional uncertainties is still a work in progress, with no results shown here.

The uncertainty for pitching moment was developed as a function of Mach and total angle of attack using Equations 2 and 3 from the previous section. The database requires that the uncertainties in pitching and yawing moment be provided as functions of α and β for the operating space of the vehicle. The transformations applied to $uC_m(\alpha_T)$ to get $uC_m(\alpha, \beta)$ and $uC_n(\alpha, \beta)$ have evolved over several iterations of the database release cycle. It has been problematic to develop a consistent formulation, primarily because there is not a reasonable estimate of $uC_n(\alpha_T)$ due to data limitations. For the most recent database release, covering $M < 8$, the method for developing moment uncertainties in the full (α, β) space was reworked to provide a more intuitive formulation starting with the basic pitching moment magnitude uncertainty as a function of α_T. Both a decrease in the basic pitching moment uncertainty and the reformulation led to a reduction in the yawing moment uncertainties.

The typical sine/cosine transformation from $uC_m(\alpha_T)$ to $uC_m(\alpha, \beta)$ and $uC_n(\alpha, \beta)$ has issues at $\alpha = 0°, 180°$. The yawing moment uncertainty is identically zero here (suggesting no lateral asymmetry in the vehicle), and the sign of the pitching moment uncertainty changes when crossing $\alpha = 0°, 180°$, both physically unrealistic situations that led to problems with trajectory simulations. As a result, the database was reformulated to provide $uC_m(M, \alpha, \beta)$ and $uC_n(M, \alpha, \beta)$ directly. Developing those tables was challenging, and has been done inconsistently for different sections of the database. The current formulation attempts to provide a clear methodology to go from the (relatively) easily developed $uC_m(\alpha_T)$ to the full $uC_m(\alpha, \beta)$ and $uC_n(\alpha, \beta)$ by considering the relevant boundary and symmetry assumptions that can be made in the transformation and applying some engineering judgement to set thresholds that are not easily determined from the data. The uncertainties are first formulated in (α_T, ϕ), in order to provide an uncertainty on both the magnitude and direction of the total moment uncertainty. In order to formulate the final uncertainties as a function of (α, β), a Monte-Carlo-like process is used to vary the magnitude and direction of the total moment uncertainty. This process is then applied to the current $uC_m(\alpha_T)$ uncertainties to provide the desired $uC_m(\alpha, \beta)$ and $uC_n(\alpha, \beta)$ uncertainties for the database tables.

V. Results

Several aspects of the final database are explored in this section. The final nominals and uncertainties are compared to the experimental and computational data for selected Mach numbers to provide a sense of how well the database models the data. The trends in Mach number at selected angles of attack are presented to give a sense of how the vehicle aerodynamics change during entry. Finally, a discussion of how the database uncertainties contribute to trim angle-of-attack and drag dispersions is presented. These examples of the final database and how it is used serve to show the overall scope of the database development and reveal areas that can be improved upon.

V.A. Force and Moment Comparisons, Angle-of-attack Trends

The final nominal aerodynamic coefficients with their associated uncertainty bands are compared to the available experimental and computational data for selected Mach numbers to provide a general overview of the final aerodatabase. Figure 33 shows the aerodynamic coefficients for $M = 0.5$ over the full angle-of-attack range. In general, the nominals were developed from the experimental data (cyan symbols) and IDAT computational data (orange diamonds). CFD data for the nominal backshell angle (blue symbols) for both wind tunnel and flight conditions as well as the USM3D IDAT computations (purple) are shown to provide a reference for the code-to-code variation and Reynolds number coverage provided in the uncertainties. The increased uncertainty in the vicinity of $\alpha = 60°$ is evident for C_L and $C_{m_{cg}}$. The trim region for the same condition is shown in Figure 34, for C_D and $C_{m_{cg}}$. The large variation in the CFD data is evident, with the uncertainties not fully covering the CFD data. This is expected based on the fact that the CFD data was ignored in the trim region for the nominal development, but reinforces the need for improved reliability of CFD methods for this type of flowfield. Note also the reduction in uncertainty for the pitching moment as the angle-of-attack approaches 180°.

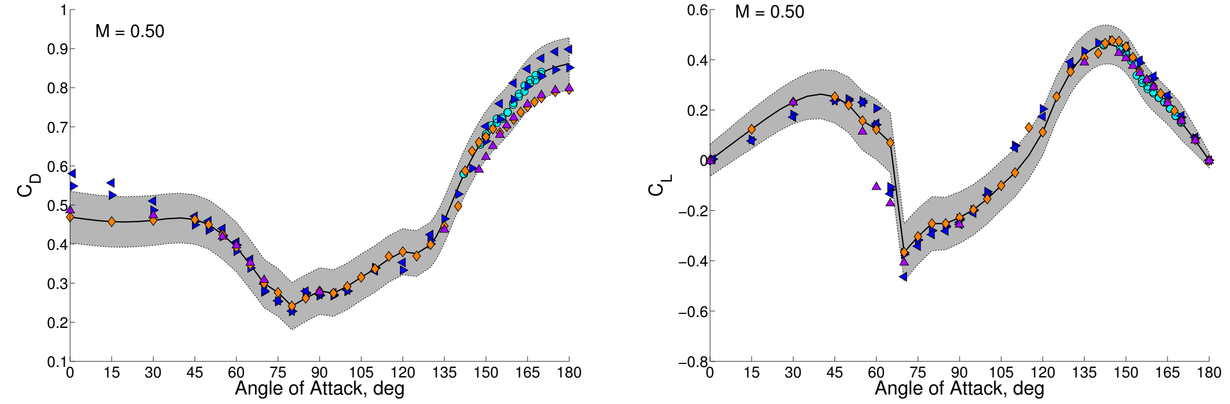

(a) C_D

(b) C_L

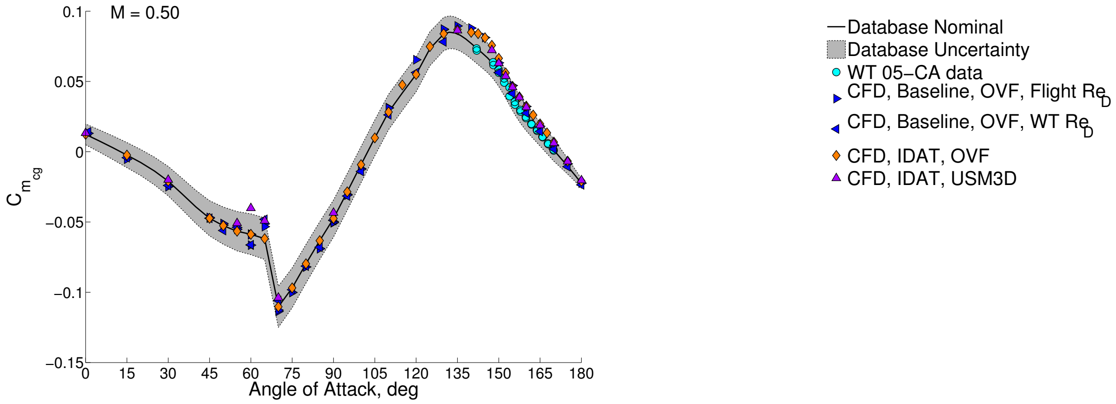

(c) $C_{m_{cg}}$

(d) Legend

Figure 33: Nominal aerodynamic coefficients with uncertainties compared to available experimental and computational data, for $M = 0.50$.

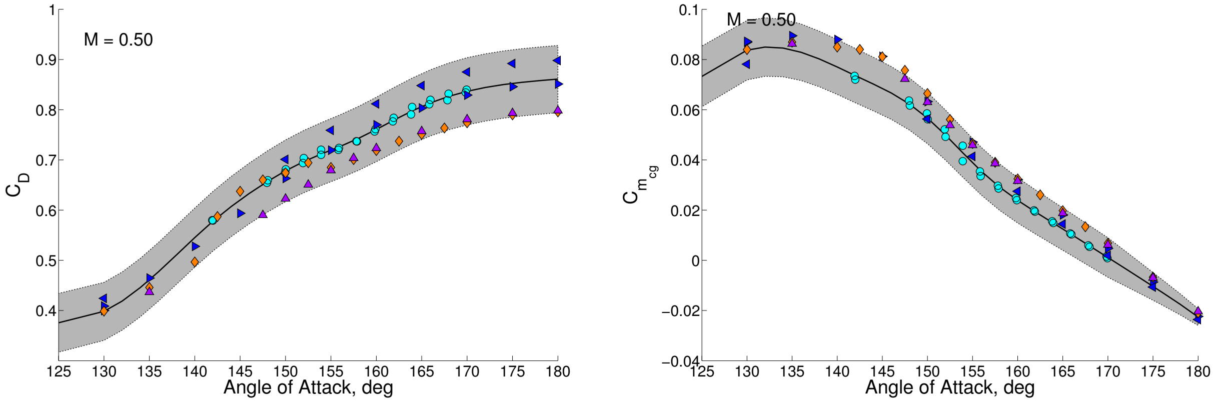

(a) C_D

(b) $C_{m_{cg}}$

Figure 34: Nominal aerodynamic coefficients with uncertainties compared to available experimental and computational data, for $M = 0.50$, trim angle of attack region. See Figure 33(d) for the legend.

The format of Figure 33 is repeated in Figure 35 for $M = 1.2$ and Figure 36 for $M = 2.5$. The uncertainties are reduced substantially for C_L and $C_{m_{cg}}$; C_D uncertainty remains high for $M = 1.2$. There is not a steep gradient in C_L or $C_{m_{cg}}$ at the higher Mach numbers near $\alpha = 60°$ as was seen for the subsonic Mach numbers. The uncertainty band fully encompasses the data in the trim region above $M = 1.4$; Figure 37 shows this for C_D and $C_{m_{cg}}$ at $M = 2.5$.

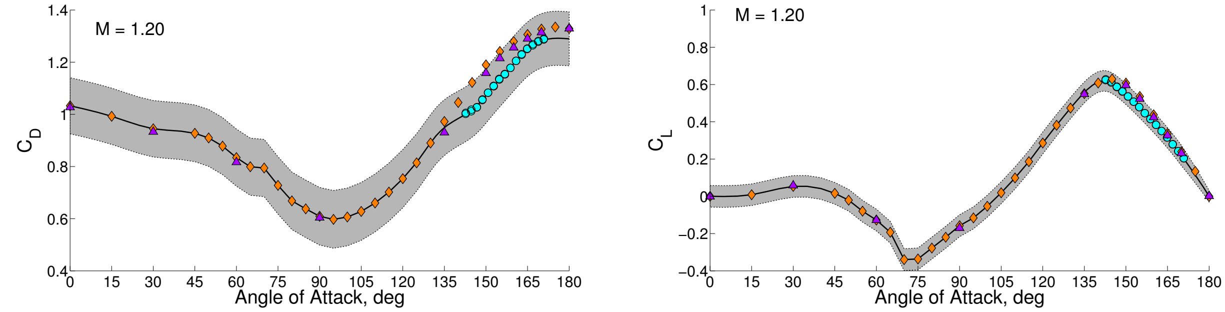

(a) C_D

(b) C_L

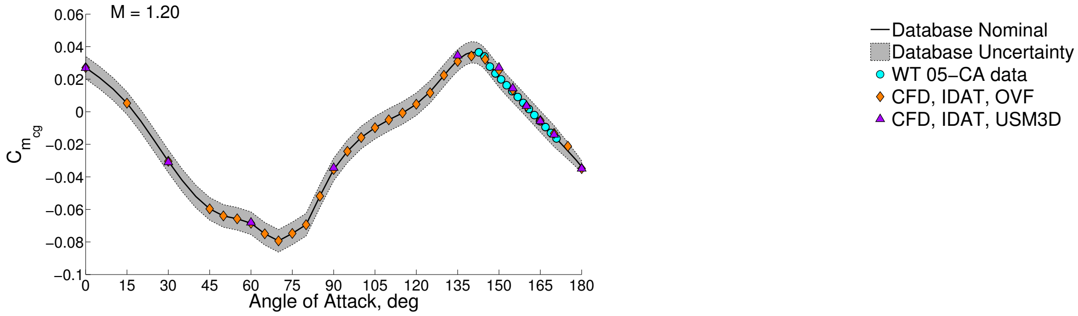

(c) $C_{m_{cg}}$

(d) Legend

Figure 35: Nominal aerodynamic coefficients with uncertainties compared to available experimental and computational data, for $M = 1.2$.

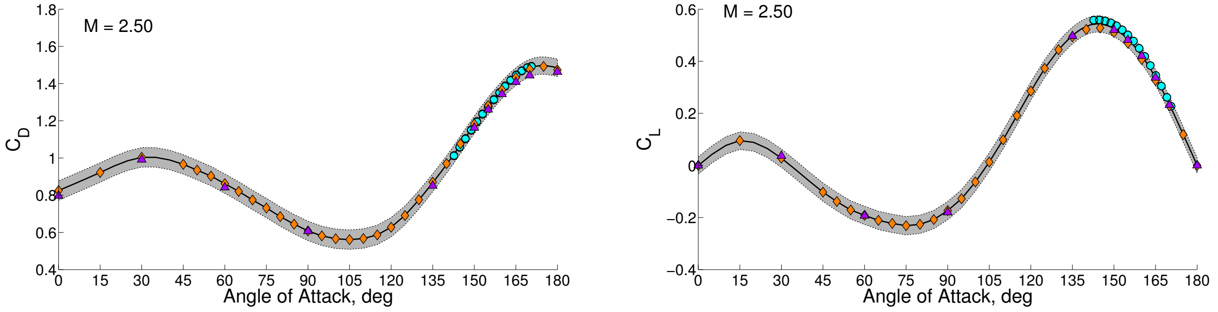

(a) C_D (b) C_L

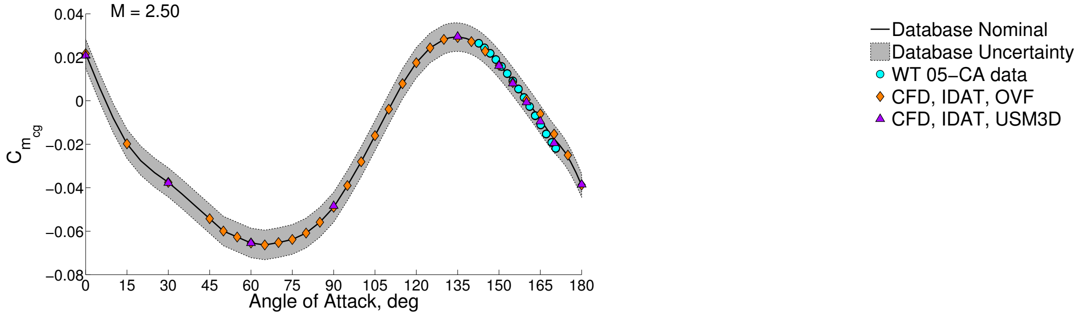

(c) $C_{m_{cg}}$ (d) Legend

Figure 36: Nominal aerodynamic coefficients with uncertainties compared to available experimental and computational data, for $M = 2.5$.

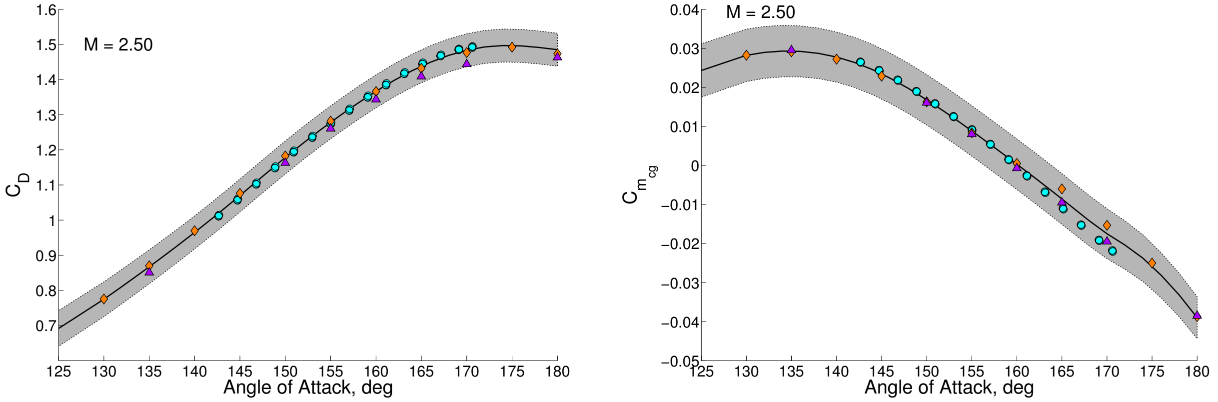

(a) C_D (b) $C_{m_{cg}}$

Figure 37: Nominal aerodynamic coefficients with uncertainties compared to available experimental and computational data, for $M = 1.2$, $\alpha > 125°$. See Figure 36(d) for legend.

V.B. Mach Number Trends

To show how the uncertainties change over the Mach number range, Figure 38 shows the aerodynamic coefficients at $\alpha = 166°$ plotted vs. Mach number for the full Mach number range, and again in Figure 39 for $M < 2$. It is clear that the trends in the uncertainty magnitudes are not smooth in Mach number. This is a consequence of developing the uncertainties independently at each Mach number rather than using some type of response surface, and is not a desireable feature for providing smooth trajectory simulations. This is an area that will be examined closer for the next release of the Orion Aerodatabase.

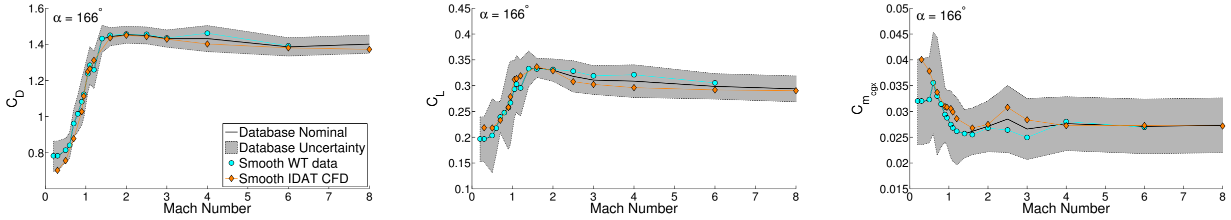

(a) C_D (b) C_L (c) $C_{m_{cg}}$

Figure 38: Nominal aerodynamic coefficients with uncertainties compared to available experimental and computational data, for $\alpha = 166°$, $M < 8$

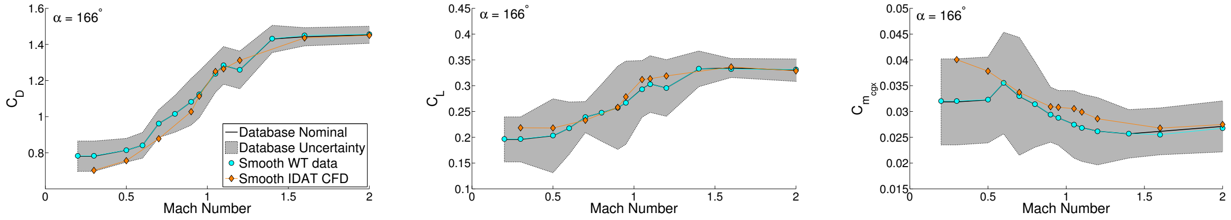

(a) C_D (b) C_L (c) $C_{m_{cg}}$

Figure 39: Nominal aerodynamic coefficients with uncertainties compared to available experimental and computational data, for $\alpha = 166°$, $M < 2$.

V.C. Trim Angle and C_D Variation

At the lower Mach numbers, drag is a more important parameter than L/D for vehicle performance. In particular, the minimum subsonic drag is an important factor in sizing the landing parachutes. The uncertainty in drag in flight is affected by the uncertainty in C_D as well as the uncertainty in the trim angle of attack. In the companion paper,[7] there is a lengthy discussion on the various uncertainty parameters that affect trim angle of attack and lift-to-drag ratio. Figure 40(a) shows the nominal trim angle for $M < 4$. The various symbols show the trim angle when different levels of uncertainty in pitching moment, lift, drag, and *cg* location are applied. It is important to note that, for the nominal *cg* location used in these calculations, the trim angle of attack gets as high as 175°. This is well beyond the maximum angle of attack for the experimental data used to develop the aerodatabase, and reflects the shift in the nominal CM *cg* location over the course of the vehicle development. The dispersed C_D is shown in Figure 40(b). Note that even with the full dispersions, the subsonic drag is roughly between 0.7 and 0.9, which is below the historical Apollo flight data.

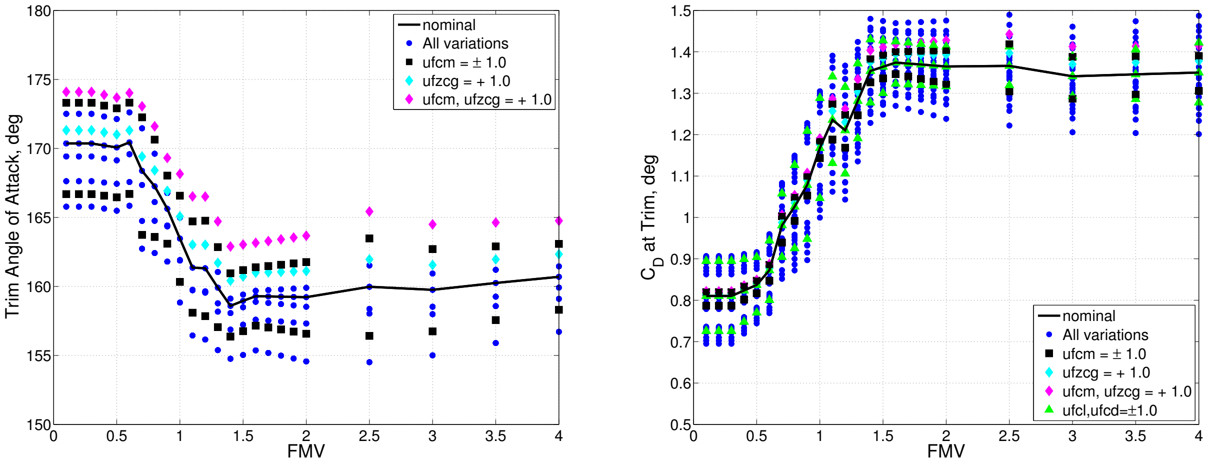

(a) Trim angle of attack

(b) C_D

Figure 40: Trim angle of attack and C_D bounds when pitching moment, *cg* location, lift, and drag are dispersed.

VI. Concluding Remarks and Future Work

This work describes the process of developing the nominal static aerodynamic coefficients and associated uncertainties for the Orion Crew Module (CM) for Mach 8 and below. The database was developed from wind tunnel test data for the baseline geometry and computational simulations of the expanded backshell CM geometry, both with no asymmetries or protuberances. The database covers the full range of Reynolds number seen in both nominal flight and ascent abort scenarios. The basic uncertainties were developed as functions of Mach number and total angle of attack from variations in the primary data as well as computations at lower Reynolds numbers, on the baseline geometry, and using different flow solvers. The resulting aerodynamic database represents the best estimate of the nominal aerodynamics for the current CM vehicle.

Several weakness in the current database development have been noted, and represent areas for future efforts that will improve characterization of the vehicle aerodynamics and reduce the uncertainties. Reynolds number effects for the subsonic region are not validated. This deficiency is being addressed on the experimental side with a test in Langley's National Transonic Facility that will capture flight Reynolds number aerodynamics. Continuing efforts are being made to improve the computational simulations of blunt bodies with highly separated flows. The formulation of the lateral-directional uncertainties is being refined to provide a more rigorous physical formulation. Additional aerothermal computational solutions are being developed that will enable refinement of the uncertainties above Mach 2.

Acknowledgments

The authors would like to acknowledge the efforts of the CAP Aerodynamic and Aerothermal Teams for developing all of the experimental and computational data used in the database development over the past 5 years. Particular thanks are due to Tuan Troung and Jim Greathouse at Johnson Space Center and Jim Ross at Ames Research Center for guiding and coordinating the experimental and computational efforts and to Grant Palmer (Ames Research Center, Aerothermal Smooth Body OML Working Group) for coordinating development and delivery of the aerodynamic data from the Smooth Body OML WG. The authors would also like to thank Sara McNamara (JSC, GNC Ascent Abort Mode Team), Jeremy Rea (JSC, GNC Entry Abort Mode Team Lead), and Bruce Owens (Langley, CAP and Launch Abort System Office) for their assistance with the trajectory plots herein.

References

[1] NASA, `http://www.nasa.gov/mission_pages/constellation/orion/`, last accessed 05 June 2011.

[2] NASA, "Orion Next Generation Spacecraft," `http://www.nasa.gov/pdf/491544main_orion_book_web.pdf`, last accessed 05 June 2011.

[3] NASA, `http://www.nasa.gov/exploration/systems/mpcv/`, last accessed 05 June 2011.

[4] NASA, "Preliminary Report Regarding NASAs Space Launch System and Multi-Purpose Crew Vehicle," `http://www.nasa.gov/pdf/510449main_SLS_MPCV_90-day_Report.pdf`, January 2011, last accessed 05 June 2011.

[5] CAP Aerodynamics Team, "Orion Aerodynamic Databook, Version 0.60.0, Volume 1," NASA CXP-72167, January 2011.

[6] CAP Aerodynamics Team, "Formulation of the Orion Aerodynamic Database," CEV Aerosciences Project EG-CEV-06-37, Rev. 0.60.0, Rev. 1, NASA Johnson Space Center, Houston, TX, October 2009.

[7] Bibb, K. L., Walker, E. L., Brauckmann, G. J., and Robinson, P. E., "Development of the Orion Crew Module Static Aerodynamic Database, Part I: Hypersonic," 29th AIAA Applied Aerodynamics Conference, Honolulu, HI, 27-30 June 2011, American Institute of Aeronautics and Astronautics, Reston, VA (submitted for publication).

[8] Bell, J., "Test 5-CA Final Report," CEV Aerosciences Project EG-CEV-06-19, NASA Ames Research Center, Moffett Field, CA, March 2006.

[9] Murphy, K., "Test 3-CA Final Report," CEV Aerosciences Project EG-CEV-06-137, NASA Langley Research Center, Hampton, VA, February 2006.

[10] Murphy, K. J., Bibb, K. L., Brauckmann, G. J., Rhode, M. N., Owens, B., Chan, D. T., Walker, E. L., Bell, J. H., and Wilson, T. M., "Orion Crew Module Aerodynamic Testing," 29th AIAA Applied Aerodynamics Conference, Honolulu, HI, 27-30 June 2011, American Institute of Aeronautics and Astronautics, Reston, VA (submitted for publication).

[11] Brauckmann, G., "Final Report for CEV Test 9-CA: Mach 6, 0° to 180° Hypersonic Aerodynamics," CEV Aerosciences Project 2006-152, NASA Langley Research Center, Hampton, VA, November 2006.

[12] Rhode, M. N., Chan, D. T., Niskey, C. J., and Wilson, T. M., "Aerodynamic Testing of the Orion Launch Abort Tower Separation with Jettison Motor Jet Interactions," 29th AIAA Applied Aerodynamics Conference, Honolulu, HI, 27-30 June 2011, American Institute of Aeronautics and Astronautics, Reston, VA (submitted for publication).

[13] Owens, D. B., "27-AD Subsonic-Transonic Launch Abort Vehicle Dynamic Stability Test in the NASA LaRC Transonic Dynamics Tunnel," CEV Aerosciences Project EG-CAP-08-79, NASA Langley Research Center, Hampton, VA, September 2010.

[14] Owens, D. B. and Aubuchon, V. V., "Overview of Orion Crew Module and Launch Abort Vehicle Dynamic Stability," 29th AIAA Applied Aerodynamics Conference, Honolulu, HI, 27-30 June 2011, American Institute of Aeronautics and Astronautics, Reston, VA (submitted for publication).

[15] Wilson, T. M., "61-AA LAS Jettison Motor and Proximity Wind Tunnel Test for PA-1 and ALAS 11 Rev 3c at the Langley 14x22 Facility," CEV Aerosciences Project EG-CEV-09-5, NASA Johnson Space Center, Houston, TX, March 2009.

[16] Nichols, R. H. and Buning, P. G., "User's Manual for OVERFLOW 2.1," Report, NASA Langley Research Center, Hampton, VA, April 2009.

[17] Nichols, R. H., Tramel, R. W., and Buning, P. G., "Solver and Turbulence Model Upgrades to OVERFLOW 2 for Unsteady and High-Speed Applications," AIAA Paper 2006-2824, June 2006, AIAA 36th Fluid Dynamics Conference, San Francisco, CA.

[18] Tramel, R. W., Nichols, R. H., and Buning, P. G., "Addition of Improved Shock-Capturing Schemes to OVERFLOW 2.1," AIAA Paper 2009-3988, June 2009, 19th AIAA Computational Fluid Dynamics Conference, San Antonio, TX.

[19] Chaderjan, N. M. and Olsen, M. E., "CEV CFD simulation guidelines for the USM3D solver," CEV Aerosciences Project EG-CAP-06-33, version 1.3, August 2006, Ames Research Center.

[20] Frink, N. T., Pirzadeh, S., Parikh, P., Pandya, M. J., and Bhat, M. K., "The NASA Tetrahedral Unstructured Software System," *Aeronautical Journal*, Vol. 104, No. 1040, pp. 491–499.

[21] Pandya, M. J., Frink, N. T., Abdol-Hamid, K. S., Parlette, E. B., and Taft, J. R., "Enhancements to TetrUSS for NASA Constellation Program," AIAA Paper 2011–1111, May 1995.

[22] Frink, N. T. and McMillan, S. N., "CEV CFD simulation guidelines for the USM3D solver," CEV Aerosciences Project EG-CAP-06-34, version 1.03, October 2006, Langley Research Center.

[23] Cheatwood, F. M. and Gnoffo, P. A., "User's Manual for the Langley Aerothermodynamic Upwind Relaxation Algorithm (LAURA)," NASA TM 4674, April 1996.

[24] Mazaheri, A., Gnoffo, P. A., Johnson, C. O., and Kleb, B., "LAURA Users Manual: 5.3-48528," NASA TM 2010-216836, August 2010.

[25] Candler, G. V., Wright, M. J., and McDonald, J. D., "Data–Parallel Lower–Upper Relaxation Method for Reacting Flows," *AIAA Journal*, Vol. 32, No. 12, 1994, pp. 2380–2386.

[26] Wright, M. J. and Candler, G. V., "The Solution of the Navier-Stokes Equations Using Gauss-Seidel Line Relaxation," *Computers and Fluids*, Vol. 17, No. 1, pp. 135–150.

[27] Wright, M. J., Candler, G. V., and Bose, D., "Data–Parallel Line Relaxation Method for the Navier–Stokes Equations," *AIAA Journal*, Vol. 36, No. 9, 1998, pp. 1603–1609.

[28] Aerodynamic Analysis Group, North American Aviation, I., "Aerodynamic Data Manual for Project Apollo," SID 64-174C, January 1965, revised February, 1966.

[29] William C. Moseley, J., Robert H. Moore, J., and Hughes, J. E., "Stability Characteristics of the Apollo Command Module," NASA TN D-3890, March 1967.

[30] Hillje, E. R., "Entry Flight Aerodynamics From Apollo Mission AS-202," NASA-TN D-4185, October 1967, MSC-PA-R-68-1, Supplement 1, TRW NOTE NO. 68-FMT-615.

[31] Bolling, L., "Apollo 6 Entry Postflight Analysis," NASA-TM-X 69719, December 1968, MSC INTERNAL NOTE NO. 68-FM-299.

[32] Skerbetz, F. G., "Apollo 7 Entry Postflight Analysis," NASA-TM-X 69740, May 1969, MSC INTERNAL NOTE NO. 69-FM-89.

[33] Snowden, J. C., “Data Report for Ames UPWT Test, Apollo Model FS-2 Static Force Model to Evaluate the Block II Command Module and Canard Launch Escape Vehicle (Ames IX),” NASA-CR 118538, October 1965, Also SID 65-1195.

[34] North American Aviation, “Data Report for Apollo Model 0.105-Scale FS-2 in the North American Aviation Trisonic Wind Tunnel TWT 79,” NASA-CR 117704, December 1962, Also SID 62-1216.

[35] North American Aviation, Apollo Engineering Aerodynamics Section, “Data Report for Apollo Model (FS-2) in NAA Trisonic Wind Tunnel (TWT 80),” NASA-CR 117713, December 1962, Also SID 62-1212-R1.

[36] North American Aviation, “Data Report for Apollo Model (FS-1) Wind Tunnel Test (Ames 2x2 - 396),” NASA-CR 116752, August 1962, Also SID 62-1027.

[37] Stremel, P. M., McMullen, M. S., and Garcia, J. A., “Computational Aerodynamic Simulations of the Orion Crew Module,” 29th AIAA Applied Aerodynamics Conference, Honolulu, HI, 27-30 June 2011, American Institute of Aeronautics and Astronautics, Reston, VA (submitted for publication).

[38] McMillin, S. N., Frink, N. T., Kerimo, J., Ding, E., Nayani, S., and Parlette, E. B., “Contributions of TetrUSS to Project Orion,” 29th AIAA Applied Aerodynamics Conference, Honolulu, HI, 27-30 June 2011, American Institute of Aeronautics and Astronautics, Reston, VA (submitted for publication).

[39] Mathworks, “Curve Fitting Toolbox 2.2,” `http://www.mathworks.com/products/curvefitting/`, 2010, last accessed 01 July 2010.

[40] “U.S. Guide to the Expression of Uncertainty in Measurement,” Tech. Rep. ANSI/NCSL Z540-2-1997, October 1997.

[41] Wheeler, D. and Chambers, D., *Understanding Statistical Process Control, 2nd ed.*, SPC Press, Knoxville, 1992.

[42] Wheeler, D., *Advanced Topics in Statistical Process Control*, SPC Press, Knoxville, 1995.

[43] Wheeler, D., *Range Based Analysis of Means*, SPC Press, Knoxville, 2003.

[44] Harter, H., “Tables of Range and Studentized Range,” *The Annals of Mathematical Statistics*, Vol. 31, No. 4, December 1960, pp. 1122–1147.

[45] Hemsch, M. J., Tuttle, D., Houlden, H., and Graham, A., “Measurement of Force Balance Repeatability and Reproducibility in the NTF,” AIAA Paper 2004-0771, January 2004.

[46] Cunningham, B., “Analysis of the 1.5 inch MK13A Task Balance,” Tech. Rep. WN-06-001, NASA Ames Research Center, Moffett Field, CA, January 2006, Ames Balance Calibration Lab Report.

[47] Ulbrich, N. and Bader, J., “Analysis of Sting Balance Calibration Data Using Optimized Regression Models,” AIAA Paper 2009-5372, August 2009.

[48] Chan, D. T., “Final Report for Test 83-AA High Reynolds Number Test of the Unpowered Launch Abort Vehicle in the NASA LaRC National Transonic Facility,” CEV Aerosciences Project EG-CAP-09-54, NASA Langley Research Center, Hampton, VA, May 2009.